^{1}H NMR Characterization of the Solution Active Site Structure of Substrate-Bound, Cyanide-Inhibited Heme Oxygenase from *Neisseria meningitidis*: Comparison to Crystal Structures†

Yangzhong Liu,‡ Xuhong Zhang,§ Tadashi Yoshida,§ and Gerd N. La Mar*,‡

Department of Chemistry, University of California, Davis, California 95616, and Department of Biochemistry, Yamagata University School of Medicine, Yamagata, Japan 990-9585

Received March 23, 2004; Revised Manuscript Received May 27, 2004

ABSTRACT: Heme oxygenase, HO, from the pathogenic bacterium *Neisseria meningitidis* catabolizes heme for the iron necessary for infection. The enzyme, labeled HemO, exhibits less sequence homology to mammalian HO than another studied HO from *Corynebacterium diphtheriae*. Solution ^{1}H NMR has been utilized to define the active site molecular and electronic structure of the cyanide-inhibited, substrate-bound complex for comparison with those provided by several crystal structures. Extensive assignments by solely ^{1}H NMR 2D methods reveal a structure that is very strongly conserved with respect to the crystal structure, although ^{1}H/^{2}H exchange indicates dynamically much more stable distal and proximal helices than those for other HOs. Several residues found with alternate orientations in crystal structures of water- and NO-ligated complexes were shown to occupy positions found solely in the NO complex, confirming that there are structural accommodations in response to ligating the substrate complex with a diatomic, H-bond acceptor ligand. The observed dipolar shifts allow the determination of the magnetic axes that show that the Fe−CN unit is tilted ∼10° toward the α-meso position, thereby facilitating the α-stereoselectivity of the enzyme. Numerous labile protons with larger than usual low-field bias are identified and, in common with the other HO complexes, shown to participate in an extended, distal side H-bond network. This H-bond network orders several water molecules, most, but not all, of which have been detected crystallographically. A series of three C-terminal residues, His207−Arg208−His209, are not detected in crystal structures. However, ^{1}H NMR finds two residues, His207 and likely Arg208 in contact with pyrrole D, which in crystal structures is exposed to solvent. The nature of the NOEs leads us to propose a H-bond between the proximally oriented His207 ring and the carboxylate of Asp27 and a salt-bridge between the terminus of Arg208 and the reoriented 7-propionyl carboxylate. While numerous ordered water molecules are found near both propionates in the crystal structure, we find much larger water NOEs to the 6- than 7-propionate, suggesting that water molecules near the 7-propionate have been expelled from the cavity by the insertion of Arg208 into the distal pocket. The conversion of the 7-propionate link from the N-terminal region (Lys16) to the C-terminal region (Arg208) in the ligated substrate complex both closes the heme cavity more tightly and may facilitate product exit, the rate-limiting step in the enzyme activity.

Heme oxygenase (HO)[1] is an enzyme that catalyzes the conversion of heme to α-biliverdin, iron, and CO in a multistep process that requires three O_2, seven electrons and nine protons (*1*). In mammals, two isoforms of HO, designated as HO-1 and HO-2, have been established (*2*, *3*). The molecular mass of HO-1 is 33 kDa and that of HO-2 is 36 kDa. HO-2 has an extra N-terminal 20-amino acids compared to the sequence of HO-1. Both enzymes are bound to microsomes with the C-terminal hydrophobic region consisting of ∼25 amino acid residues (*2*). The truncated form of both enzymes with deleted hydrophobic regions are soluble, remain fully active, and allow effective characterization of the molecular and electronic structures and catalytic mechanism (for reviews, see refs *3*−*5*). HO also occurs in several pathogenic bacteria (*6*, *7*), where its purpose appears to be to mine the host heme for the iron necessary for infection (*8*). The soluble, ∼210 residue HOs exhibit variable sequence homology (*6*, *9*, *10*) to the more extensively studied mammalian HOs, with that from *Corynebacterium diphtheriae*, called HmuO (*6*), sharing ∼35% sequence identity and high homology, particularly in the active site, while that from *Neisseria meningitidis*, named HemO (*7*), exhibits only ∼25% sequence identity and substantial differences in the key distal helix. Photosynthetic systems also possess a

† This research is supported by the National Institute of Health (GM 62830 to GNL) and by grants-in-aid from the Ministry of Education, Science, Sports, and Culture, Japan (14580641 to T.Y.). The bacterial expression vector pMW172 was a gift from Dr. K. Nagai, MRC Laboratory of Molecular Biology, Cambridge, UK.

* To whom correspondence should be addressed. Tel.: (530) 752−0958. Fax: (530) 752−8995. E-mail: lamar@indigo.ucdavis.edu.

‡ University of California, Davis.

§ Yamagata University School of Medicine.

[1] Abbreviations: HemO, heme oxygenase from *N. meningitidis*; HmuO, heme oxygenase from *C. diphtheriae*; HemO−PH−CN, protoheme-bound, cyanide inhibited HemO.; HO, heme oxygenase; hHO-1, human heme oxygenase isozyme 1; PH, protohemin; DSS, 2,2-dimethyl-2-silapentane-5-sulfonate; NOE, nuclear Overhauser effect; NOESY, two-dimensional nuclear Overhauser spectroscopy; TOCSY, two-dimensional total correlation spectroscopy;.

10.1021/bi049438s CCC: $27.50
Published on Web 07/14/2004

soluble HO in which the product biliverdin is a starting point for the construction of linear, light-sensing tetrapyrrole pigments (*11*). The mechanism of action worked out (*3*−*5*, *12*, *13*) for mammalian HO-1 is presumed to be the same for all HOs and has been shown (*12*, *14*, *15*) to involve a ferric hydroperoxy intermediate, rather than the ferryl species common to cytochromes P450 (*16*).

Crystal structures of both substrate-bound (*17*−*21*) and substrate-free (*22*, *23*) complexes of human HO-1, hHO-1, and rat HO-1, rHO-1, as well as the substrate complexes of the bacterial complexes of HemO (*24*, *25*) and HmuO (*26*), have been reported and reveal a common, primarily α-helical fold for the four HOs that account in large part for the α-meso stereospecificity of the reaction by the distal helix backbone sterically blocking all but the α-meso position. Both crystallographic (*18*, *20*, *21*, *25*, *26*) and spectroscopic data (*27*−*31*), moreover, show that axial ligands tilt or bend toward the α-meso position due to steric interaction with the distal helix, thereby providing an additional control that favors cleavage of the α-meso position. The crystal structures also find an unusually large number of ordered water molecules within the enzymes (*17*, *18*, *20*, *22*, *24*−*26*), several of which interact directly with bound ligands and have been proposed to stabilize the hydroperoxy species and serve as proton sources to the active site.

Parallel solution ^{1}H NMR studies of both substrate-bound, cyanide-inhibited hHO-1 (*28*−*30*) and HmuO (*31*), hHO-1-PH−CN (PH = protoheme) have revealed a strong steric tilt of the ligand toward the α-meso position that is confirmed crystallographically for the rat HO-1-PH−CN complex (*21*). These studies also established the presence (*30*, *32*, *33*) of an extensive H-bond network in the distal pocket, involving both backbone and side chain labile protons, that extends from the immediate environment of the bound ligand to the protein surface on the opposite side of the heme binding site. Many of the labile proton donors in the network of hHO-1 exhibited low-field chemical shifts indicative of significantly stronger H-bonds than that found in the majority of folded proteins (*30*, *33*, *34*).[2] A very similar H-bond network was identified in HmuO (*31*). Moreover, sizable, negative ^{1}H nuclear Overhauser effects, NOEs, from water to both slowly exchanging labile H-bond donor protons (*32*), and some aromatic side chains (*33*) revealed the presence of numerous ordered water molecules (*35*) in both hHO-1 and HmuO. For the most part, the ^{1}H NMR-detected (*32*, *33*) water molecules correspond closely with those detected crystallographically (*18*), and include the water molecule H-bonded to the conserved, key Asp (140 in hHO-1 (*36*), and rHO-1 (*37*)) and the distal ligand. The placement of these ordered water molecules (*18*, *26*, *30*, *33*) suggest their role as a pathway for the controlled funneling of protons to the active site.

To date, similar ^{1}H NMR studies of a HemO complex have not been reported. Because of the lower sequence homology (*7*), including substitutions for the major portion of the residues involved in the H-bond network and the distal helix and the presence of many fewer vacancies (*24*, *25*) in the distal pocket relative to hHO-1 (*18*, *24*), rHO-1 (*20*, *21*) and HmuO (*26*) complexes, the pattern of H-bonds and their interaction with ordered water molecules in HemO is likely different than that in hHO-1 or HmuO complexes. The crystal structures of HemO−PH−H_2O and reduced HemO−PH−NO have been reported (*24*, *25*) and reveal essentially the same structures except for the orientations of several distal pocket side chains. It is not known whether these structural differences reflect the different ligands (water, a H-bond donor, vs NO, a H-bond acceptor) or the different oxidation state of the iron and if they are functionally relevant. Neither the N-terminal (Met1-Gln7) nor C-terminal (His207-His209) residues are detected in the crystal structures (*24*, *25*). While the former are relatively remote from the heme, the latter, in fact, could be close to the heme and may serve a functional role. Our goals in this study are to assign and structurally characterize the active site of HemO−PH−CN for comparison with the two crystal structures, to facilitate future comparative ^{1}H NMR studies on mutated HemO complexes, to determine whether the Fe−CN is tilted toward the α-meso position to facilitate stereoselectivity as in other HO complexes (*21*, *30*, *31*), to provide information on the H-bonding pattern among distal residues and the interaction between these residues and ordered water molecules, and to probe the heme environment near the C-terminal residues.

EXPERIMENTAL PROCEDURES

Construction of HemO Expression Vector, pMWHemO. Plasmid purification, subcloning, and bacterial transformations were performed by standard procedures (*38*). A 50-base pair double-stranded synthetic oligonucleotide with unique restriction enzyme sites for NdeI, BstBI, SacI, BssHII, and Hind III was ligated between NdeI and HindIII sites of a T7-promotor-based bacterial expression vector, pMW172, to make a plasmid tentatively referred to as pMW-A. Eight and their complements, 79−96 nucleotides in length, were synthesized to construct a 630-base pair synthetic gene coding the entire HemO from the ATG initiation codon to the TAA stop codon. Each nucleotide was phosphorylated with T4 polynucleotide kinase then annealed with its complement to make a double-stranded DNA (e.g., Oligo I to OligoVIII. Oligo I and Oligo II were designed so that the 5′ end of Oligo I could be ligated to the NdeI site), whereas its 3′ cohesive end was complementary to the 5′ end of Oligo II. The 3′ end of Oligo II could be ligated to the BstBI site. Similarly, the 5′ ends of Oligos III, V, and VII were designed to ligate to the BstBI, SacI, and BssHII sites, respectively, and their 3′ ends had sequences for ligation to the 5′ ends of Oligo IV, VI, and VIII, respectively. The 3′ end of Oligo IV, VI, and VIII had sequence for ligation to SacI, BssHII, and Hind III sites, respectively. To complete the HemO expression vector, pMWHemO, double stranded Oligo I to Oligo VIII were ligated step by step into the restriction enzyme sites of pMW-A. The nucleotide sequence of the thus constructed pMWHemO was determined by an Applied Biosystems 373A DNA sequencer.

Protein Expression and Purification. A 5-mL inoculum in Luria-Bertani medium (+50 μg/mL ampicillin/0.1% glucose) was prepared from a plate of transformed *Escherichia coli* BL21 (DE3) cells carrying pMWHemO. Cultures (500 mL) of Luria-Bertani medium (+200 μg/mL ampicillin) were inoculated with 100 μL of the inocula and grown at 37 °C until $A_{600\ nm}$ reached 0.8−1.0. The cells were grown for an additional 16 h at 25 °C, harvested by centrifugation, and stored at −80 °C until use. The harvested cells were

[2] BioMagResBank (http://www.bmrb.wisc.edu).

blue rather than green. The typical yield of cells from a 500-mL culture was 1.3 g.

The *E. coli* cells (10 g), resuspended into 90 mL of Tris-HCl buffer (pH 7.4, +2 mM EDTA), were lysed (2 mg of lysozyme/g of cells) with stirring at 4 °C for 30 min. After sonication (Branson 450 Sonifire) and cetrifugation at 100000*g* for 1 h, the resulting supernatant was covered into a 40−65% ammonium sulfate fraction and centrifuged. The subsequent precipitates, containing the HemO protein, were dissolved in 20 mM K-phosphate buffer (pH 7.4) and applied to a Sephadex G75 column (3.6 × 50 cm), preequilibrated with the same buffer. The protein fractions eluted in the K-phosphate buffer tinged with blue were collected and directly loaded onto a DE−52 column (2.6 × 28 cm). After washing the column with 50 mL of 20 mM K-phosphate (pH 7.4)-50 mM KCl, the protein was eluted with 400 mL of 20 mM K-phosphate (pH 7.4) using a linear gradient, 50−250 mM KCl. At this step, the blue color (residual biliverdin) was retained in the column, and the resulting eluant was a clear, colorless solution. Collected fractions with intense 24 kDa band of SDS−PAGE were further run through a hydroxylapatite column (2.6 × 20 cm). The protein was eluted with 400 mL of K-phosphate (pH 7.4) using a linear gradient, 20−200 mM. Only fractions with the single band at 24 kDa on SDS−PAGE were finally gathered. About 25 mg of protein was obtained from 1 L of culture. The protein concentrations were estimated by Lowry's method using crystalline bovine serum albumin as standard (*39*).

Reconstitution of HemO with Hemin. To obtain the complex of heme and HemO, we added excess (1.2-fold in terms of molar concentration) hemin to HemO and chromatographed the mixture on Sephadex G-25 and DE−52 column. Samples were prepared ~2.5 mM in 95% ^1H2O/5% ^2H_2O, 100 mM in phosphate, 30 mM in KCN at pH 7.4. A ^1H_2O sample was converted to ^2H_2O by column chromatography, as described previously (*34*, *40*).

NMR Spectroscopy. ^1H NMR data were collected on Bruker AVANCE 500 and 600 spectrometers operating at 500 and 600 MHz, respectively. Reference spectra were collected in both ^1H_2O over the temperature range 15−35 °C at a repetition rate of 1 s^{-1} using a standard one-pulse sequence, as well as with 3:9:19 "soft" pulse detection (*41*) with and without saturation of the water solvent signal. Steady-state NOE difference spectra were generated from the 3:9:19 spectra with on-resonance and off-resonance saturation of the desired signals. WEFT spectra (*42*) were recorded to emphasize strongly relaxed resonances (repetition rate 10 s^{-1}, relaxation delay 5−50 ms). Chemical shifts are referenced to 2,2-dimethyl-2-silapentane-5-sulfonate (DSS) through the water resonance calibrated at each temperature. Nonselective T_1s were determined in both ^1H_2O and ^2H_2O at 20, 25, and 30 °C from the initial magnetization recovery of a standard inversion−recovery pulse sequence. The distance of a given proton, H_i, from the iron, R_{H_i}, was estimated from the relation $R_{H_i} = R^*_{Fe}[T_1^*/T_{1i}]^{1/6}$, using the heme α-*meso*-H for H^* ($R^*_{Fe} = 4.6$ Å and $T_1^* = 60$ ms) as reference. Selective T_1s were estimated from the initial decay of the diagonal peak intensity in 3:9:19 NOESY spectra (where the solvent resonance is completely suppressed (*41*)) as a function of mixing time. 600 MHz NOESY (*43*) with both hard-pulse and 3:9:19 detection (*41*) spectra (mixing time, 40 ms; 15−35 °C) and 500 MHz Clean-TOCSY (to suppress ROESY response (*44*)) spectra (25, 35 °C, spin lock 25 and 40 ms) using MLEV-17 (*45*) were recorded over a bandwidth of 25 kHz (NOESY) and 12 kHz (TOCSY) with recycle times of 500 ms and 1 s, using 512 t1 blocks of 128 and 256 scans, each consisting of 2048 t2 points. 2D data sets were processed using Bruker XWIN software on a Silicon Graphics Indigo workstation and consisted of 30°- or 45°-sine-squared-bell-apodization in both dimensions, and zero-filling to 2048 × 2048 data points prior to Fourier transformation.

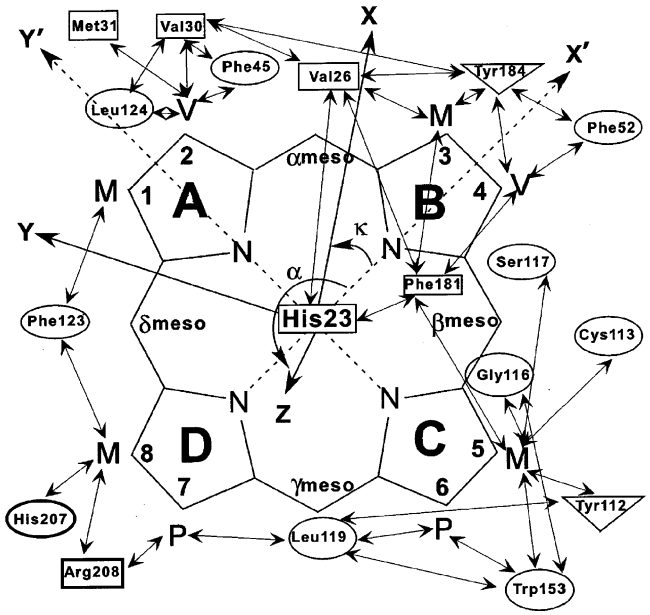

FIGURE 1: Schematic representation of the heme and proximal (rectangles), distal (circles) and equatorial (triangle) residues whose NOESY cross-peaks (indicated by double-sided arrows) indicate the expected (*24*, *25*), and observed, heme contacts. Two unexpected heme contact residues are shown in bold. The reference coordinate system, *x*′, *y*′, *z*′, based on crystal coordinates, as well the magnetic coordinate system *x*, *y*, *z*, where the paramagnetic susceptibility tensor is diagonal, are shown. The magnetic axes are related to the reference axes by the Euler transformation, Γ(α, *β*, *γ*), with (*x*, *y*, *z*) = (*x*′, *y*′, *z*′) Γ(α, *β*, *γ*), where *β* is the tilt of the major magnetic axes, *z*, from the heme normal (*z*′), α gives the direction of tilt, as defined by the projection of the *z*-axis on the heme plane relative to the *x*′ axis, and the angle $\kappa \approx \alpha + \gamma$ defines the rhombic magnetic axes, *x*, *y*′, relative to the *x*′, *y* axis. The −*z* direction correlates with the Fe−CN tilt.

Magnetic Axes Determination. The location of the magnetic axes were determined by finding the Euler rotation angles, Γ(α,*β*,*γ*), that rotate the crystal-structure based, iron-centered reference coordinate system, *x*′, *y*′, *z*′, into the magnetic coordinate system, *x*, *y*, *z*, where the paramagnetic susceptibility tensor, *χ*, is diagonal where α, *β*, *γ* are the three Euler angles (*29*−*31*, *46*, *47*). The angle *β* dictates the tilt of the major magnetic axis, *z*, from the heme normal *z*′, α reflects the direction of this tilt, and is defined as the angle between the projection of the *z* axis on the heme plane and the *x*′ axis (Figure 1), and $\kappa \approx \alpha + \gamma$ is the angle between the projection of the *x*, *y* axes onto the heme plane and locates the rhombic axes (Figure 1). The magnetic axes were determined by a least-squares search for the minimum in the error function (*30*, *46*−*48*)

$$F/n = \sum_{i=1}^{n} |\delta_{dip}(\text{obs}) - \delta_{dip}(\text{calc})|^2 \qquad (1)$$

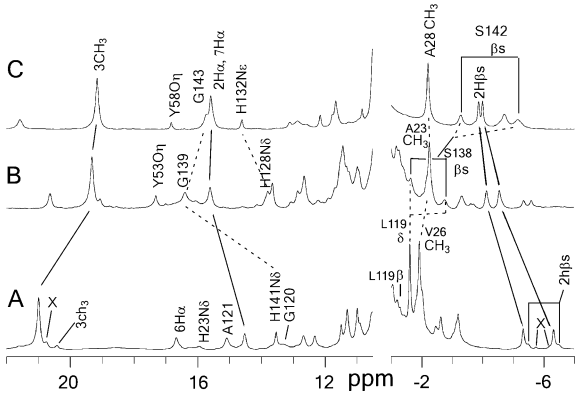

FIGURE 2: The resolved portions of the 600 ^{1}H NMR spectrum of (A) HemO−PH−CN, (B) HmuO−PH−CN, and (C) hHO−1-PH−CN, all at pH ∼7.4, 100 mM phosphate in ^1H_2O at 30 °C. Peaks in A are labeled as determined herein, and those in B and C are labeled as reported previously (*29*, *31*). Solid vertical lines connect the heme resonances in the three complexes and dashed lines connect the homologous upfield, proximal helix, and low-field, distal helix residues in the three complexes.

where the calculated dipolar shift in the reference coordinate system, x', y', z', or R, θ', Ω', is given by

$$\delta_{dip}(calc) = (24\pi N)^{-1}[2\Delta\chi_{ax}(3\cos^2\theta' - 1)R^{-3} + 3\Delta\chi_{rh}(\sin^2\theta'\cos^2\Omega')R^{-3}]\Gamma(\alpha, \beta, \gamma) \quad (2)$$

with $\Delta\chi_{ax}$ and $\Delta\chi_{rh}$ as the axial and rhombic anisotropies of the diagonal paramagnetic susceptibility tensor. The observed dipolar shift, δ_{dip}(obs) is given by

$$\delta_{dip}(obs) = \delta_{DSS}(obs) - \delta_{DSS}(dia) \quad (3)$$

where δ_{DSS}(obs) and δ_{DSS}(dia) are the chemical shifts, in ppm, referenced to DSS, for the paramagnetic hHO-1-hemin CN complex and an isostructural diamagnetic complex, respectively. In the absence of an experimental δ_{DSS}(dia), it may be reliably estimated (*29*, *31*) from the available molecular structure (*24*, *25*)

$$\delta_{DSS}(dia) = \delta_{tetr} + \delta_{sec} + \delta_{rc} \quad (4)$$

where δ_{tetr}, δ_{sec}, and δ_{rc} are the chemical shifts of an unfolded tetrapeptide relative to DSS (*49*), the effect of secondary structure[3] (*50*, *51*), and ring currents (*52*) on the shift, respectively.

RESULTS AND DISCUSSION

Comparison to Other HO−PH−CN Complexes. The resolved portions of the 600 MHz ^{1}H NMR spectrum of equilibrated HemO−PH−CN in ^1H_2O are illustrated in Figure 2A, with the crowded low-field and high-field portions expanded in Figures 3A and 4A, respectively. Peaks are labeled as assigned herein. The resonances arise predominantly from one major species (>90%), with two sets of minor component peaks detected. Those marked 3-ch$_3$ and 2h$_\beta$s (∼5%) in Figure 2A represent the heme orientation reversed by 180° about the α−γ-meso axis (*28*, *31*, *53*) The peak 3CH$_3$ and 3ch$_3$ are comparably intense upon initially adding protohemin, followed by CN$^-$, to apo-HemO but lose intensity with a half-life of ∼1.5 h at 25 °C and pH 7.1. Another set of peaks, marked by X in Figure 2A, appear in variable amounts upon addition of protohemin, followed by cyanide. Moreover, over very long times (weeks to months), the major isomer appears to convert to this minor isomer (not shown). The nature of this latter minor isomer is not

[3] The program provided by ref *51* was used to obtain the $\delta_{tetr} + \delta_{sec} + \delta_{rc}$ for all but aromatic rings, whose shifts were determined by the program described in ref *50*. The effect of the heme ring current was determined by the program described in ref *52* in all cases.

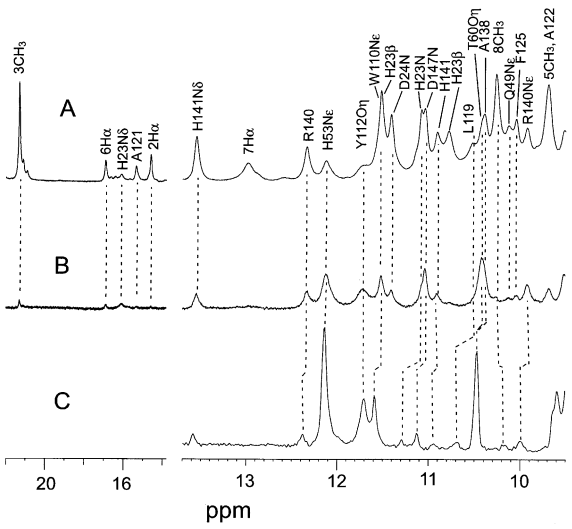

FIGURE 3: (A) Low-field, resolved portions of the "3:9:19" 600 MHz ^{1}H NMR reference spectrum (*41*) (without water saturation, and with the carrier at 13 ppm) of HemO−PH−CN in ^1H_2O, 100 mM in phosphate at 25 °C and pH 7.4. Peaks are labeled as determined herein. (B) "3:9:19" steady-state NOE difference spectra upon saturating the water resonances at 25 °C. (**C**) Low-field portion of the 3:9:19 NOESY F2 slice through the water signal at 18 °C.

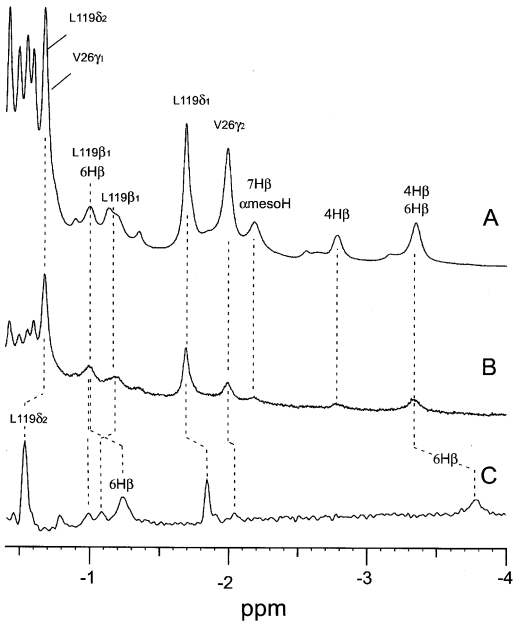

FIGURE 4: (A) Portion of the resolved, high-field "3:9:19" ^{1}H NMR reference spectrum (without water saturation and with carriers at 13 ppm) of HemO−PH−CN in ^1H_2O, 100 mM in phosphate at pH 7.1 and at 25 °C; peaks are labeled as assigned herein. (B) "3:9:19" steady-state NOE difference spectrum at 25 °C upon saturating the water resonance at 25 °C; the vertical scale is ×2 relative to the reference trace in A. (C) Upfield portions of the F2 slices through the water signal of "3:9:19" NOESY (τ_m = 40 ms) spectra (without water saturation) at 18 °C.

Table 1: Chemical Shifts for the Heme and Axial His for HemO−PH−CN, HmuO−PH−CN and hHO-1-PH−CN

Heme	HemO[a]	hHO-1[b]	HmuO[c]
1-CH_3	7.90	4.95	4.91
2H_α	14.48	15.68	15.63
2H_βs	−5.58, −6.62	−4.22, −4.23	−4.35, −4.80
3-CH_3	21.40	19.63	19.65
4H_α	8.06	10.09	9.87
4H_βs	−2.80, −3.38	1.77, 2.52	0.43, 0.80
5-CH_3	9.62	9.04	8.09
6H_αs	16.92, 1.14[d]	11.75, 10.62	10.12, 9.59
6H_βs	−1.02, −3.38[d]	0.40, 0.40	−0.74, −1.00
7H_αs	13.06, 5.73[d]	15.87, 5.68	11.64, 7.57
7H_βs	−1.10, −2.17[d]	−0.45, −0.45	−0.52, −0.66
8-CH_3	10.33	10.48	10.37
α-meso-H	−2.21	−5.10	−3.63
β-meso-H	8.13	7.60	
γ-meso-H	−1.82	3.84	
δ-meso-H	6.43	7.13	7.24
Axial His[e]			
N_pH	11.08	10.46	10.03
C_αH	7.37	4.86	4.01
C_βHs	11.56, 10.75	9.77, 10.31	9.24, 9.99
Ring	16.1 (N_δ), 19.4 (C_ϵ)		

[a] Shifts in ppm, referenced to DSS, in ^1H_2O, 100 mM in phosphate, pH 7.4 at 25 °C. [b] Shifts in ppm, referenced to DSS, in ^1H_2O 100 mM phosphate at pH 8.4; taken from ref *31*. [c] Shifts in ppm, referenced to DSS, in ^1H_2O 100 mM in phosophate, pH 7.1 at 25 °C, taken from ref *29*. [d] Propionate proton closer to the adjacent methyl on the same pyrrole. [e] His23 in Hem O, His20 in Hmu O, and His25 in hHO-1.

Table 2: Chemical Shifts for Residues with Significant Dipolar Shifts[a]

Residue	NH	αs	*β*s	other
Thr19	8.04	5.52	5.75	1.70(*γ*), 5.9(O_γ)
Thr20	8.37	6.30	5.14	2.27(*γ*), 6.35 (O_γ)
Ala21	9.36	5.31	2.04	
Val22	9.44	4.87	2.72	1.50, 1.40
Asp24	11.41	6.80	3.65, 4.30	
Ser25	8.77			
Val26	8.33	2.80	1.60	−1.96(*γ*1), 0.51(*γ*2)
Val30	7.87	2.46	0.40	−0.68(*γ*1), −0.21 (*γ*2)
Met31	7.29			
Tyr112	8.19			6.57(*δ*), 6.62(*ϵ*), 11.68(O_η)
Cys113	7.40	2.60	2.32, 2.04	−0.19(S*γ*)
Ala114	8.04	3.71	1.60	
Glu115	9.07	4.01		
Gly116	7.95	0.49, 0.55		
Ser117	6.12			
Asn118	8.46	7.83	3.94, 3.62	
Leu119	10.54	4.72	−1.15, −0.95	−0.40(*γ*), −1.69(*δ*1), −0.63(*δ*2)
Gly120	13.60	5.75		
Ala121	15.32	8.52	5.44	
Ala122	9.73	4.93	1.98	
Phe123	8.83	4.51	3.46, 3.27	7.07(*δ*), 6.94(*ϵ*)
Phe125	10.00	4.47		7.50(*δ*), 7.40(*ϵ*)
Leu142	7.23	5.30	2.39, 2.09	0.60(*δ*)
Trp153		4.34	3.00, 2.90	6.37(*δ*1), 8.69(*ϵ*1), 7.09(*ϵ*3), 6.43(z2), 5.87(z3), 6.09(*η*2)
Phe181	7.82			7.25(*δ*), 7.72(*ϵ*), 8.87(*ζ*)
Tyr184				5.20(*δ*), 5.35(*ϵ*), 7.44(OH)
His207[b]		4.04(e)	2.22(c), 2.43(d)	6.81(*δ*), 7.63 (*ϵ*)
Arg208[b]		3.84(e)		1.02(a), 1.54(b)

[a] Shifts in ppm, referenced to DSS via the residual solvent peak, at 25 °C in ^1H_2O solvent 100 mM in phosphate at pH 7.4. [b] Peaks as labeled in Figure 6, parts A−C.

understood, but has been determined[4] not to represent an alternative heme orientation in the pocket. We concern ourselves here only with the initially found major isomer. The spectrum of HemO−PH−CN in Figure 2A can be compared with those of HmuO−PH−CN (*31*) and hHO-1-PH−CN (*29*, *33*) in Figure 2, parts B and C, respectively. The similarity of the spectra, particularly for heme resonances, is striking. Moreover, the homologous distal helix residue side chain over the heme pyrrole C,D junction (Ser142 in hHO-1, Ser138 in HmuO, Leu119 in HemO) appear similarly upfield shifted, while the homologous distal helix residue near the iron (Gly143 in hHO-1, Gly139 in HmuO, and Gly120 in HemO) are similarly relaxed and appear well downfield. Several of the resolved or partially resolved signals in HemO−PH−CN exhibit significant paramagnetic relaxation (T_1 < 100) ms, indicating close proximity to the iron (R_{Fe} < 5 Å). The upfield, partially resolved signals with $T_1 \sim 55-60$ ms are to be identified as α-meso-H and *γ*-meso-H (R_{Fe} ~4.5 Å) and three labile proton peaks at 16.1 ppm ($T_1 \sim 30$ ms, R_{Fe} ~4 Å), 15.32 ppm ($T_1 \sim 60$ ms; R_{Fe} ~4.5 Å) and 13.60 ppm (T_1 ~20 ms; R_{Fe} ~4.8 Å) arise from a His N_δH and two peptide NHs, respectively, while the broad, nonlabile proton peaks of indeterminate intensity at 19.4 ppm (T_1 < 5 ms) will be shown to arise from a His ring CH.

Resonance Assignments. Target residues include the heme, those paramagnetically influenced near the heme pocket, those that participate in robust H-bonds, as characterized by relatively low-field shifted labile protons (*30*, *34*, *54*), and residues that participate in inter-aromatic or aromatic−aliphatic contacts that probe the tertiary structure of the enzyme. Extensive use of variable temperature 2D NMR data greatly improve resolution (*30*, *47*, *55*) for both hyperfine shifted and labile protons in H-bonds and confirm uniqueness of both dipolar and scalar contacts. Crystal structures for two derivatives have been reported (*24*), HemO−PH−H_2O and reduced HemO−PH−NO (*25*), and have shown that, while the overwhelming majority of the structure, in particular the proximal side, are conserved, both some distal helix residues and heme itself exhibit different side chain orientations in the two structures. Hence, to the degree allowed by line width and resolution, we assign resonance sequence-specifically, independent of the crystal structure, by their characteristic backbone connection (*56*), the most prominent of which are the N_i-N_{i+1}, α_i-N_{i+1}, β_i-N_{i+1}, α_i-N_{i+3}, and/or $\alpha_i-\beta_{i+3}$ dipolar contact characteristic of an α-helix. Upon assignment of the heme and proximal helix, the magnetic axes will be determined using the proximal side δ_{dip}(obs) and proximal helix crystal coordinates as input. The remainder of the target residues are assigned using the predicted dipolar shifts, distance estimates from relaxation, and the two crystal structures as guides. The chemical shift for the heme and residues with significant dipolar shifts that provide the magnetic axes and probe structure are listed in Tables 1 and 2, respectively. Similar data on other assigned residues are provided in Supporting Information. Since the assignment protocols for similar HO complexes have been presented in detail previously (*29*−*31*, *33*), we illustrate ^1H NMR data primarily to provide information of structural difference between solution and crystal. Other 2D data are provided in Supporting Information.

[4] Liu, Y.; Zhang, X.; Yoshida, T.; and La Mar, G. N.; unpublished data.

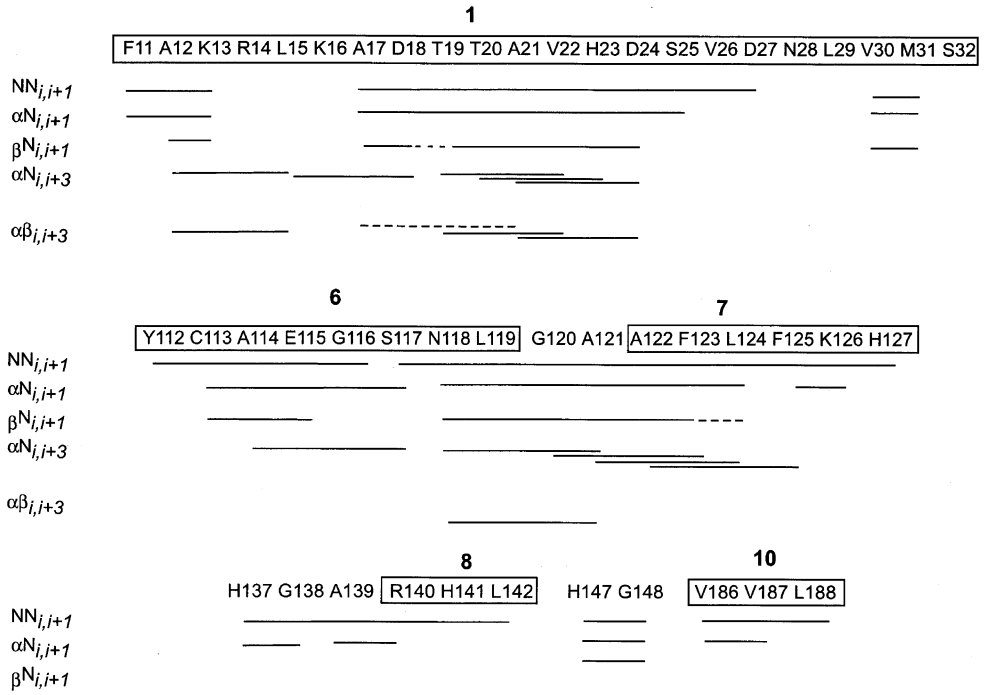

FIGURE 5: Schematic representation of backbone NOESY connectivities for sequence-sequentially assigned residues of HemO−PH−CN.

The Heme. The complete heme, including the four meso-Hs and stereospecific differentiation of methylene protons, are unambiguously assigned following standard procedures as reported for both isoelectronic globins (*47*, *57*) and other HO complexes (*29*−*31*). The chemical shifts are listed in Table 1 where they can be compared with similar data for the hHO-1 (*29*) and HmuO complexes (*31*). The pattern of the heme substituent hyperfine shifts, which are dominated by the contact interaction (*47*), is very similar to that reported for hHO-1-PH−CN (*29*) and HmuO−PH−CN (*31*), with large π spin density at positions 2, 3, 6, and 7, and is that expected for an axial His imidazole plane oriented approximately along the $\beta-\delta$-meso line (*47*, *58*), as observed in the crystal structure of all three HO substrate complexes (*17*, *18*, *24*−*26*). The observed (not shown; see Supporting Information) steeper than Curie (T^{-1}) behavior for the 2-, 3-, 6- and 7-hyperfine shifts, and the antiCurie behavior for 1-, 5-, and 8-CH_3 hyperfine shifts is consistent with thermal populations of the excited spin doublet with an in-plane 90° rotated magnetic axes (*47*, *59*).

The Proximal Helix. Typical backbone NOESY connections (summarized schematically in Figure 5) among TOCSY-detected spin system reveal the helical fragment $Ala_i-AMX_{i+1}-Thr_{i+2}-Thr_{i+3}-Ala_{i+4}-Val_{i+5}-AMX_{i+6}-AMX_{i+7}-(N)_{i+8}-Val_{i+9}$, which the sequence uniquely identifies as a part of the proximal helix 1 consisting of Ala17-Val26. An additional fragment, $(\alpha N)_j-Ala_{j+1}-N_{j+2}$... Leu_{j+4}, with typical helical contacts (aromatic ring in contact with $(\alpha N)_j$) and a $\alpha_{j+4}-N_{i+1}(\alpha_{15}-N_{18})$ NOESY peaks identifies a further segment of the proximal helix with predicted contacts of Phe11, Ala12, and Leu15 with Leu160, Asn161, and Val157 (see Supporting Information). AMX_{i+6} must arise from the axial His23, as is confirmed by large low-field $C_\beta H$ contact shifts typical for a His ligated to low-spin ferric heme (*47*) (Table 1). Thr19, Thr20 and Asp24 exhibit significant downfield dipolar shifts, and Leu15 and Val26 exhibit significant upfield dipolar shifts. Strong dipolar contacts are observed between the methyls of Val26 and the heme 3-CH_3 and 2-vinyl, and between Val26 and axial His23 (summarized schematically in Figure 1), as expected from the crystal structures (*24*, *25*). A strongly relaxed and low-field shifted labile proton that exhibits significant saturation transfer from water displays NOESY cross-peaks to the Asp24 $C_\alpha H$ and NH, as well as to the $C_\beta Hs$ of His23 (not shown, see Supporting Information). These contacts identify it as the axial His23 $N_\delta H$, a proton that has not been detected in either hHO-1-PH−CN (*30*, *60*) or HmuO−PH−CN (*31*) at the same temperature and pH. Hence, the exchange rate in HemO−PH−CN is significantly slower (> factor ~10) than that in the other complexes. A low-field shifted and relaxed three-spin aromatic ring exhibits NOESY cross-peaks to His23 $C_\beta Hs$, the Thr19 $C_\beta H$, and (weakly) to 3-CH_3 and 2-vinyl, and moderately to 5-CH_3 (see Figure 6F) as expected solely for the ring of Phe181. Last, a severely relaxed ($T_1 \leq$ 5 ms), nonlabile proton peak of indeterminate intensity at 19.4 ppm fails to exhibit NOESY cross-peaks, but saturation of the peak in ^2H_2O (see Supporting Information) leads to NOEs to the $C_\epsilon H$ and $C_\zeta H$ of the assigned Phe181 ring, as well as to the 5-CH_3. These NOEs and the crystal structure dictate that at least one component of this strongly relaxed proton peak arises from the $C_\epsilon H$ of the axial His23.

The Magnetic Axes. Determination of the orientation of the magnetic axes using the anisotropies ($\Delta\chi_{ax} = 2.48 \times 10^{-8}$ m^3/mol, $\Delta\chi_{rh} = -0.58 \times 10^{-8}$ m^3/mol) previously determined for a variety of iso-electronic cyanide complexes of ferric globins (*47*, *61*) and hHO-1−PH−CN (*29*−*31*, *47*) (and shown to be highly conserved among low-spin His/cyanide-ligated ferric hemins) (*47*), and the proximal residue crystal coordinates from HemO−PH−NO (IP3U; (*25*)) leads to $\alpha = 257°$, $\beta = 10°$, and $\kappa = 38°$ and a good fit between δ_{dip}(obs) and δ_{dip}(calc), as shown in the open data points in Figure 7. Essentially the same result is obtained when using the HemO−PH−H_2O crystal structure (not shown). We now use the δ_{dip}(calc) for distal residues, predicted by these

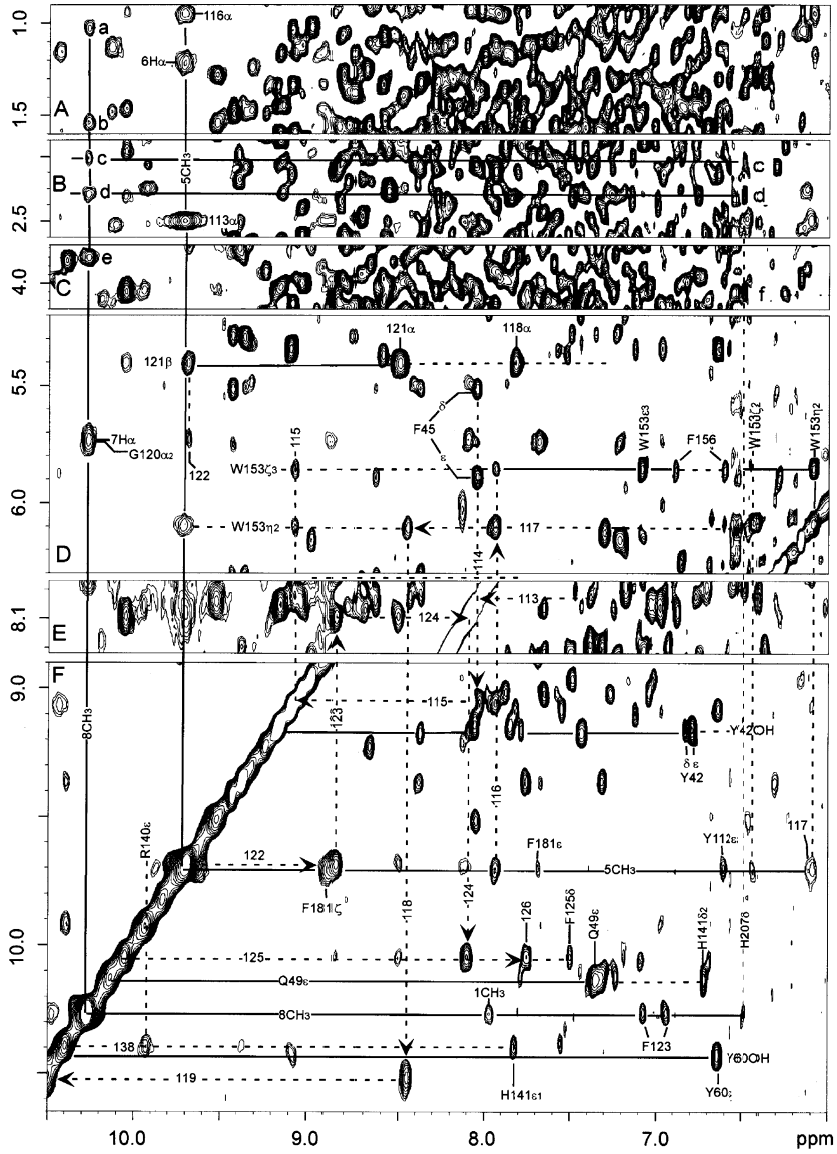

FIGURE 6: Portions of the 600 MHz ^{1}H NMR NOESY spectrum (mixing time 40 ms) of HemO−PH−CN in ^1H_2O, 100 mM in phosphate, pH 7.4 at 25 °C illustrating contacts between the 8-CH_3 and Arg208 (A, C), 8-CH3 and His207 (B, C, F), 5-CH_3, Trp153, and Gly116 (D, F), the sequential N_i-N_{i+1} connection for distal helix residues Ala114-Phe123 (D, E, F), and the His141 to Glu49 and Phe181 to 5-CH3 connection.

magnetic axes, to guide assignments and confirm conservation or perturbation of structural elements in the distal side of the heme. Included in Figure 7 are similar data observed and predicted for the distal residues of interest (closed circles).

The Distal Helix. In the crystal structures (*24*, *25*), the heme is transversed by a strongly kinked distal helix that is divided by the kink into helix 6 (Gly104-Leu119) and helix 7 (Ala122-Gln129). Characteristic sequential backbone contacts (summarized in Figure 5; data shown in Figure, parts D−F and Supporting Information) identify a fragment: (Cys/Ser)$_i$−Ala$_{i+1}$−(Nα)$_{i+2}$−(Nα)$_{i+3}$−(N)$_{i+4}$, with the labile proton for Cys/Ser resolved upfield at 35 °C (and lost in ^2H_2O). The sequence identifies this as Cys113-Gly116 and C_αHs of Ser117, a portion of helix 6, with the contacts to the 5-CH_3 (Cys113 C_αH, SH, Gly116 NH, and Ser117 NH; see Figures 6B and 6F) predicted by the crystal structure. The significant upfield shifts for Cys113 and Gly116 are reasonably well predicted by the magnetic axes (Figure 7). The NH of Ser117 is observed via the expected NOESY cross-peaks for C_αH of Gly116; the crystal structure places the Ser117 C_αH < 4 Å from the iron, rendering the NH−C_αH TOCSY/NOESY cross-peaks undetectable, and the $C_\alpha HC_\beta H_2$ fragment is predicted to resonate under the intense diamagnetic envelope. A complete Trp ring with weak upfield dipolar shifts exhibits a pattern of NOESY cross-peaks to 5-CH_3 is that as predicted for the distal Trp153 (see Figure 6F). Moreover, the NHs of both Glu115 and Ser117 NHs exhibit the expected NOESY cross-peaks (Figure 6D) to the Trp153 ring. Ala114 exhibits NOESY cross-peaks to an aromatic ring (Figure 6D) that also exhibits NOESY cross-peaks to the 4-vinyl group (not shown), as expected solely for Phe52, and to the nonlabile ring proton of a His, as expected solely for His53. The ring N_ϵH, which exhibits saturation transfer for water, is assigned on the basis of the comparable NOEs to both C_ϵH and C_δH of His53.

A second sequential fragment (Figure 5) is described by: AMX$_j$−N$_{j+1}$−(Nα)$_{j+2}$−N$_{j+3}$−Ala$_{j+4}$−AMX$_{j+5}$−(Nα)$_{j+6}$−AMX$_{j+7}$−(N)$_{j+8}$−(Nα)$_{j+9}$ (with sequential dipolar contacts summarized in Figure 5), with NH$_{j+2}$ and NH$_{j+3}$ exhibiting

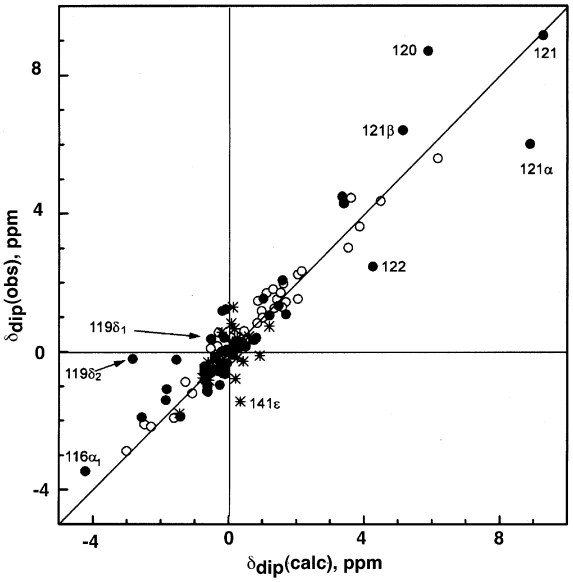

FIGURE 7: Plot of δ_{dip}(obs) and δ_{dip}(calc) for the optimized magnetic axes orientation determined on the basis of input (δ_{dip}(obs)) data for proximal residues and crystal coordinates for these residues of HemO−PH−NO, with $\alpha = 257°$, $\beta = 10°$, $\kappa = 38°$, residual $F/n = 0.33$ ppm^2 and $\Delta\chi_{ax} = 2.48 \times 10^{-8}$ m^3/mol and $\Delta\chi_{rh} = -0.58 \times 10^{-8}$ m^3/mol, the highly conserved, and the anisotropies for isostructural cyanomet myoglobin (*61*). Input data are shown as open circles, predicted distal residue data are shown as closed circles for the distal helix, and stars represent other assigned residues.

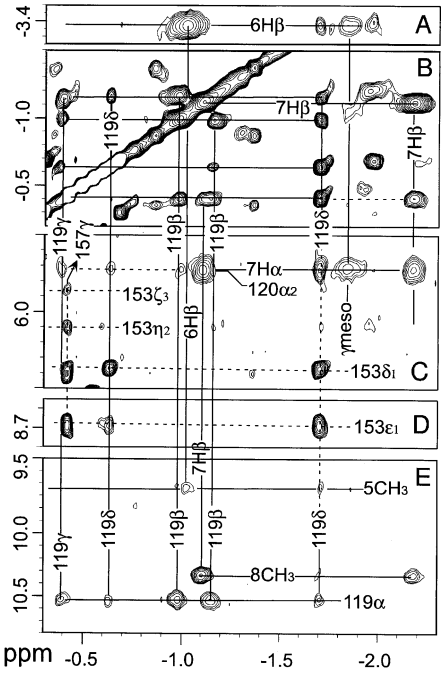

FIGURE 8: Portions of the 600 MHz ^{1}H NMR NOESY spectra (mixing time 40 ms) of HemO−PH−CN in ^1H_2O, 100 mM in phosphate, pH 7.4 at 25 °C illustrating contacts among propionate protons (A−D), between propionates protons and heme methyls (E, F), between Leu119 and Trp153 (D, E) and between Leu119 and heme propionates and methyls (C, D, F).

severe relaxation (Figure 2A). The sequence identifies this as Asn118-Phe125 and part of the backbone of Asn126-His127 (N_i-N_{i+1} connectivity in Figure 6, parts D and F), and part of helix 7. This fragment is contiguous to that identified above, as confirmed by the observed N_{i+4} (Ser117) to N_j (Asn118) NOESY cross-peak. A complete TOCSY-detected Leu side chain (see Supporting Information) with upfield resolved C_βHs and $C_\delta H_3$s (Figure 4, parts A and B) exhibits the NOESY cross-peaks to N_{j+1} and the adjacent residue consistent with Leu119. The Leu NH is too broad and the C_αH too close to the water signal to allow detection of the N-α TOCSY peak but is assigned by the unique NOESY contacts (Figure 8E) to its side chain (Figure 8B). Similarly, a strongly low-field shift N_{j+2} exhibits the NOESY contact to a low-field shifted, TOCSY-detected $CHCH_3$ (not shown; see Supporting Information) fragment identified the relaxed Ala121 (Figure 6D). The strong relaxation of Gly120 NH (T_1 ~30 ms) is consistent with the placement $R_{Fe} < 5$ Å, and the inability to locate the $C_{\alpha 1}$H peak is consistent with its predicted extreme relaxation (i.e., $R_{Fe} < 4$ Å). NOESY cross-peaks of an aromatic ring to the backbone AMX_{i+7} confirm Phe125 (Figure 6F), and contact of one of two weakly spin coupled aromatic protons to N_{i+9} locate the His127 ring. Sizable dipolar shifts are displayed by Asn118, Leu119, Gly120 and Ala121 (Table 2). The Asn118 C_βH dipolar contacts to Leu119 NH (not shown) are not consistent with either of the alternate orientations of Asn118 in the two crystal structures (*24*, *25*) (see below). Observed, and expected, are dipolar contacts with the heme of Leu119 with 8-CH_3 and 6-propionate and 7-propionate (see below), Gly120 to 8-CH_3, Phe123 ring to 1-CH_3, and Leu124 $C_\delta H_3$ to 3-CH_3 (see Figure 1). Not expected, but observed, are NOE of the Phe123 ring to 8-CH_3 (Figure 6F) (see below).

The reasonable correlation between δ_{dip}(obs) for distal helix residues and δ_{dip}(calc) from the magnetic axes is shown as closed circles in Figure 7. The NOESY cross-peak pattern to the heme, the dipolar shifts, and the paramagnetic relaxation argue for the backbone distal helices 6 and 7 placements relative to the heme and each other in HemO−PH−CN in solution that are very similar to the essentially indistinguishable positions in the alternate crystal structures (*24*, *25*). The Asn118 and Leu119 side chains and the 7-propionate group, whose orientations differ in the alternate crystal structure, are considered in a subsequent section.

Sequential Segments within the H-Bond Network. A fragment involves low-field labile protons with inconsequential paramagnetic relaxation and is represented by $Gly_i-Ala_{i+1}-Z_{i+2}-AMX_{i+3}-Z_{i+4}$, with sequential contacts summarized in Figure 5. Dipolar contact of AMX_{i+3} with a His ring CH, which is weakly TOCSY-coupled to another CH, confirms AMX_{i+3} as a His and identifies the fragment as Gly138-Leu142. The low-field (13.5 ppm) labile proton with no TOCSY connection exhibits a strong NOESY cross-peak to one of the two His141 ring CH, identifying it as the His141 N_δH, the adjacent C_ϵH (8.1 ppm) and C_δH (6.5 ppm). This one-turn helix is homologous to the similar helix/loop of Leu164-Phe167 in hHO-1 and Gly160-Tyr161 in HmuO. An AMX spin system exhibits strong NOESY cross-peaks to an aromatic ring and the assigned His137 C_δH and identifies Tyr133; α_{133}-N_{134} and β_{133}-N_{134} peaks locate Asp134. The sequential N_{i+1} connectivities for a $Val_i-Val_{i+1}-(\alpha N)_{i+2}$ are still detected after 1 year in ^2H_2O and uniquely identify Val186−Val187−Leu188 (Figure 5). A fragment AMX_i-Gly_{i+1} is consistent with arising from Asp147−Gly148. The correlation between δ_{dip}(obs) and δ_{dip}(calc) based on the magnetic axes is shown in Figure 7 by asterisks.

Heme Contacts and Other Residues. Having confirmed positions of the proximal and two distal helices relative to the heme that are the same as in the crystal structures, we assign herein the remaining target residues on the basis of their expected contacts to the heme and among each other as predicted in the two crystal structures and the predicted dipolar shifts. The starting point for all assignments is either a sequence-specifically assigned residue or one assigned on the basis of its confirmed contact to the heme, and assignments are considered robust only if at least two alternate routes to its assignment are observed. The pattern of predicted and observed heme-residue contacts for assigned residues is shown in Figure 1. The predicted, and observed, interresidue contacts are shown in Supporting Information. The chemical shift for these residues are listed in Supporting Information.

The patterns of observed NOESY cross-peaks to pyrrole A (Val30, Met31, Phe45, Phe123, Leu124), pyrrole B (Val26, Phe181, Tyr184), and pyrrole C (Tyr112, Cys113, Gly116, Ser117, Trp153), are those predicted by the crystal structures (*24*, *25*), confirming a strongly conserved environment of these pyrroles. The 8-CH_3, on the other hand, is predicted to make contact solely to the strongly relaxed Gly120, whose $C_{\alpha 2}H$ exhibits the expected NOESY cross-peak, as well as to the backbone of the assigned Phe123. However, the 8-CH_3 exhibits NOESY cross-peaks of significant intensity to the ring of Phe123, to numerous unassigned hyperfine shifted (as evidenced by temperature dependence shift) aliphatic protons (peaks labeled *a*−*d* in Figure 6, parts A−D) and one aromatic proton (Figure 6F) that is shown by TOCSY to arise from a His ring. Hence, pyrrole D exhibits an environment inconsistent with either crystal structure. The nature of this environment is treated in a later section. Starting with the assigned contacts to the heme and sequence-specifically assigned residues, another 40 residues were assigned (see Supporting Information) on the basis of conserved tertiary contacts. The present effort provides assignments for 84 of the 209 residues using solely homonuclear NMR, and those residues probe a large fraction of the tertiary contacts within the structure.

Distal Steric Interactions. Since the δ_{dip}(calc) for distal helix residues, determined from the magnetic axes orientation based solely on proximal residues, correlated reasonably well with the δ_{dip}(obs), it is reasonable to assume that the assigned distal pocket residues (with the exception of Asn118, Leu119, and Arg140 side chains; see below) occupy positions that are the same as those found in the two crystal structures (*24*, *25*). Both the proximal and distal residue nonlabile proton δ_{dip}(calc), with one noteworthy exception, correlate well with the temperature gradient of the δ_{DSS}(obs), (not shown; see Supporting Information), indicating that a single electronic/molecular structure accounts for the hyperfine shifts (*47*, *61*). The Leu119 side chain shifts exhibit significant deviation in this plot, indicating that the side chain likely exhibits a temperature-dependent distribution of orientations. This conclusion is consistent with the finding of different Leu119 orientations in the alternate crystal structures (*24*, *25*).

The direction and magnitude of tilt of the *z* axis from the heme normal reflects the tilt of the Fe−CN unit (*29*, *30*, *47*, *62*), (−*z* direction projects to an angle of 77° relative to *x′* axis) which is in the general direction occupied by the α-meso position in both the crystal (*24*, *25*) and solution structure of HemO (Figure 1). The ∼20° tilt in the same direction previously deduced from NMR data for hHO-1-PH−CN (*29*, *30*) has been confirmed in the crystal structure for the largely isostructural rat HO-1 complex (*21*). Inspection of the crystal structures (*24*, *25*) indicates that this ∼10° tilt in HemO−PH−CN would arise from steric interaction with the distal helix backbone. The tilt of the ligand in the general direction of the α-meso position has obvious implications for enhancing the stereospecificity of the cleavage at a specific meso-position. It is noteworthy that the HO from the bacterium *P. aeruginosa*, PigA, is unique in exhibiting altered (non α-position) stereoselectivity (*9*) relative to all other characterized HOs. This primarily δ-meso cleavage (*9*) for PigA results from simple in-plane ∼90° rotation of the heme (*63*) relative to a conserved interaction between the distal helix and heme that sterically blocks three meso positions and tilts the ligand toward the fourth meso position to be cleaved (*64*). Thus, primarily the δ-meso position in PigA occupies the position where the α-meso position is found in hHO, HmuO, and HemO complexes. The variable β- versus δ-stereoselectivity in PigA and its mutants (*9*, *65*) is rationalized by the expected (*28*, *31*, *53*) heme orientational disorder about the α−γ- axis.

Comparison to Crystal Structures. The generally reasonable correlation for distal residues between δ_{dip}(obs) and δ_{dip}(calc) based on the magnetic axes support a distal polypeptide structure conserved relative to that in the crystal structures (*24*, *25*) of either HemO−PH−H_2O or reduced HemO−PH−NO, with the exception of five side chains (see below) and the pyrrole D environment. This largely conserved distal pocket structure is further supported by the pattern of heme-residue and interresidues NOESY cross-peaks and by the paramagnetically induced relaxation. Two side chain orientations found different from those described in any of the crystal structures (*24*, *25*) is a 180° rotation about the C_β-C_γ bond of Gln49, as clearly evidenced by the NH_2 NOESY cross-peak to Phe45 (not shown) and His141 $C_\delta H$ (Figure 6F), and a 180° rotation of the His53 ring based on the NOEs to Ala114 and Phe52. The HemO−PH−H_2O (*24*) and reduced HemO−PH−NO (*25*) crystal structures differ in heme pocket with respect to the orientations of the Arg77, Asn118, Leu119, and Arg140 side chains and the 7-propionate group. All but the Arg77 side chains have been assigned, and the contacts to neighboring groups have been characterized.

The Asn118 side chain is oriented toward the heme and interacts with the ligated water in HemO−PH−H_2O (*24*) but rotates its side chain ∼180° to orient away from the heme and interact with the reoriented Arg77 side chain in HemO−PH−NO (*25*). The different Asn118 side chain orientations are characterized by one very short and one long $C_\beta H$ distance to the Leu119 NH, with the two C_βHs interchanging their proximity to Leu119 NH in the alternate crystal structures. The ^{1}H NMR data (not shown) show, in fact, that the two Asn118 C_βHs exhibit comparable NOESY cross-peak intensities to Leu119 NH. This is consistent with either an Asn118 side chain orientation intermediate between that in the alternate crystal structures or comparable population of the alternate Asn118 orientations in HemO−PH−CN. It was not possible to differentiate between these two models. The signals for the Arg77 side chains could not be located.

In the immediate distal heme cavity, two side chain orientations that differentiate the alternate crystal structures (*24*, *25*) are a ∼180° rotation about the C_β−C_γ bond of

Leu119 and a ~180° rotation about the $C_\pi-C_\alpha$ bond of the 7-propionate group. The observation of NOESY cross-peaks between the Gly120 $C_{\alpha 2}H$ and both 7-propionate H_βs (Figure 6C and Supporting Information) demands that the 7-propionate group is oriented toward the distal side (as in HemO−PH−NO (*25*)), rather than the proximal side (as in HemO−PH−H_2O (*24*)). The observed Leu119 $C_\gamma H$ NOESY cross-peak to 7-H_βs (Figure 6B and Supporting Information), but not to the Trp153 ring (Figure 6C), confirm a Leu119 orientation as in HemO−PH−NO (*25*). Last, the Arg140 side chain differs in the two crystal structures by a ~90° rotation about the $C_\alpha-C_\beta$ bond, with the terminal guanidyl group closer to the distal helix, and in position to make a H-bond with the Gly138 carbonyl solely in the HemO−PH−NO structure. An unassigned, low-field, labile proton peak at 9.92 ppm exhibits a strong NOESY cross-peak to the $C_\alpha H$ of His137 and several protons in common with the Arg140 NH, which is consistent only with the Arg140 $N_\epsilon H$ in the orientation depicted in HemO−PH−NO (*25*). NOESY cross-peaks from the Arg140 $N_\epsilon H$ to a pair of labile protons that exhibit dynamic line broadening at elevated temperature locate the adjacent $N_\eta H_2$.

Hence, we conclude that the HemO−PH−CN structure in solution much more closely resembles the structure in the crystal of HemO−PH−NO (*25*) than HemO−PH−H_2O (*24*). It is likely that the distal active site side chain reorientations observed upon converting HemO−PH−H_2O to HemO−PH−NO in the crystal (or to HemO−PH−CN in solution) reflect the process of replacing a monatomic, H-bond donor ligand (H_2O) with a diatomic, H-bond acceptor ligand (NO or CN^-) and can also be expected to characterize the reduced HemO−PH−O_2, which is too instable to allow either crystallographic or extensive spectroscopic structural characterization.

The Role of the C-Terminal Residues. The 7-propionate carboxylate participates in a salt bridge with the side chain of Lys16 in the HemO−PH−H_2O crystal structure (*24*). The salt bridge is ruptured in the HemO−PH−NO structure (*25*), with a 180° rotation of the propionate group that moves the 7-carboxylate from the proximal to the distal side, but the crystal structure does not locate the likely donor for a salt bridge. The ^{1}H NMR data on HemO−PH−CN provides some insight into this alternate salt bridge. Thus, neither crystal structure locates any side chain protons within 5 Å of 8-CH_3 except the relaxed Gly120 and the Phe123 backbone (both assigned). However, as shown in Figure 6, parts A−C, the 8-CH_3 exhibits a series of six NOESY cross-peaks (peaks *a*−*e*) to relatively narrow resonances in the aliphatic spectral window and one in the aromatic spectral window (Figure 6F), the $C_\delta H$ of a confirmed His (with minimal upfield δ_{dip}, as reflected in small temperature gradient). Both the His ring $C_\delta H$ and the 8-CH_3, moreover, exhibit NOESY cross-peaks to two aliphatic protons (peaks *c* and *d*), the possible backbone of the His (Figure 6, parts B and C) (the His $C_\delta H$ to another aliphatic proton *f* in Figure 6F). The majority of the NOESY cross-peaks to the 8-CH_3 in the aliphatic window exhibit moderate upfield dipolar shifts, as reflected by the significant temperature dependence of the shifts and identify the peaks with the strongest NOESY cross-peaks at 4.3 ppm (peak *e* in Figure 6C) as a $C_\alpha H$.

All of the His detected in the crystal structures (*24*, *25*) occur in regions of the protein whose structure in HemO−PH−CN is highly conserved relative to the crystal structures, and hence none of the His in the polypeptide sequence Ala8-Pro206 can account for the His side chain NOESY cross-peak to 8-CH_3. However, none of the crystal structures (*24*, *25*) detect the three C-terminal residues, His207-Arg208-His209. The residues Gly193-Pro206 participate in two β-turns. Even without changing the backbone configuration of the residues Gly193-Pro206, the His207 side chain can orient toward the heme on the proximal side to make contact with the 8-CH_3. The His207 side chain in this orientation is in position to form a H-bond to the proximal Asp27 carboxylate. The Arg208 side chain, moreover, can readily orient so as to place its cationic terminus on the distal side in position to serve as a donor to the 7-carboxylate. Stereoviews of these His207/Arg208 orientations are depicted in Figure 9. It is noted that these His207/Arg208 orientations place the Arg208 $C_\alpha H$, with a small upfield δ_{dip}(calc) ~0.5 ppm, within 4 Å of the 8-CH_3 and hence account for peak *e* in Figure 6D. The other side chain protons of His207 and Arg208 are the likely origins of the aliphatic proton responsible for peaks *a*−*d* and *g* in Figure 6, parts A−C, whose chemical shifts are included in Table 2. It is of interest that the residues homologous to Asp27 in other HOs (Glu29 in hHO-1 (*17*, *18*) and Glu24 in HmuO (*26*)) are oriented so as to serve as H-bond acceptors to the axial His ring $N_\delta H$. In the crystal structures of HemO (*24*, *25*), the latter role is served by the Asp24 side chain adjacent to the axial His, freeing the Asp27 side chain for interaction with His207. The unexpected Phe123 ring to 8-CH_3 NOESY cross-peak can be rationalized by small Phe123 $\alpha-\beta$ and/or $\beta-\gamma$ bond rotation, which may be in response to the insertion at Arg208 into the pyrrole D environment. Isotope labeling, considerably more assignments, and additional structural data would be needed to generate a more quantitative model.

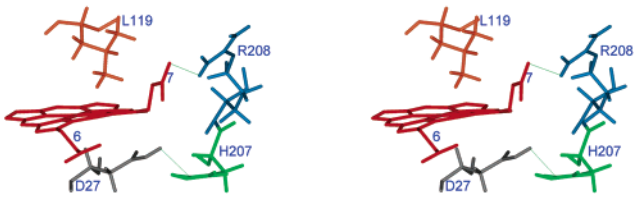

FIGURE 9: Stereoview of the heme (red), Asp27 (violet), Leu119 (orange), His207 (green) and Arg208 (blue) as modeled by the interaction between 8-CH_3 and the two side chains. The positions of the His207 and Arg208 side chain terminus allow H-bonds to the Glu27 and 7-propionate carboxylates, respectively.

Several potential functional roles for the His207/Asp27 carboxylate and Arg208/7-propionate interactions can be envisaged. First, inspection of the crystal structure shows that the 7-propionate carboxylate is oriented toward the proximal side, as in HemO−PH−H_2O (*24*), and leaves a solvent opening to the surface that is sealed with the reorientation for the 7-propionate, as found in reduced HemO−PH−NO (*25*) (not shown). The interaction which stabilizes the "closed" conformation for the 7-propionate is the interaction with Arg208, as well as the His207-Asp27 interaction. Second, the rate-limiting step in heme cleavage by all HOs is product release (*3*−*5*). Hence, the conversion of the heme 7-propionate link from an interior donor near the N-terminus (Lys16 in HemO−PH−H_2O (*24*)) to the mobile C-terminus Arg208 donor upon adding ligand may be a key step in facilitating the proper "exit" of the α-biliverdin product from the active site. In mammalian

Table 3: Residues Involved in H-bond Network and/or near Ordered Water

H-bond donor				H-bond acceptor			
residue	δ_{DSS}(obs)[a]	δ_{DSS}(dia*)[b]	$t_{1/2}$[c]	residue	r(X−H..O)[e]	∠X−H..O[f]	nearby water (Å)[g]
Ala121 N_pH	15.32		5×10^3				#141 (4.2), #74 (4.8)
His141 $N_\delta H$	13.56	13.12	10^2	Asp84 CO_2^-	2.8	164	B (3.5)
Arg140 N_pH	12.33	12.0	1.7×10^4	Asp84 CO_2^-	2.7	164	B (3.9)
His53 $N_\epsilon H$	12.13	11.4	<0.1	water #25	3.2	143	#25 (3.2)
Trp110 $N_\epsilon H$	11.52	11.5	8×10^3	water#72	2.8	158	#72 (2.8)
Tyr112 $O_\eta H$	10.68	11.7	<0.1	6-propionate	2.6	155	#26 (2.9)
Asp24 N_pH	11.41	8.1	1.8×10^3				#143 (4.4)
Asp147 N_pH	11.04	10.8	$\sim 10^4$	His145 N_δ	3.1	170	
His23 N_pH	11.08	8.8	$\sim 10^4$				#8 (4.9)
His141 N_pH	10.91	10.1	8×10^3	Asp84 CO_2^-	2.9	168	B (4.1)
Tyr60 $O_\eta H$	10.43	10.4	<0.1	Glu115 CO_2^-	2.8	170	#29 (2.9)
Gln49 $N_\epsilon H$	10.14	10.1	$\sim 10^2$	His141 N_ϵ	2.9	162	#25 (3.5), #76 (3.3)
Arg140 $N_\epsilon H$	9.92	9.8	$<10^2$	Asp81 CO_2^-	2.7	150	
Gly138 N_pH	10.38	10.0	$\sim 10^2$	Asp87 CO_2^-	3.0	174	A(2.4)
Tyr42 $O_\eta H$	9.17	9.2	$<10^2$	Gly138 C=0	2.7	170	
Tyr184 $O_\eta H$	7.44	9.1	<0.1	Gln49 O_ϵ	2.8	159	

[a] Observed chemical shift, referenced to DSS, at 25 °C. [b] Chemical shift corrected for δdip(calc) to more directly reflect H-bond strength. [c] Half-life for $X^1H \rightarrow X^2H$ exchange, in s, at 25 °C. [d] Likely acceptor, as identified in the crystal structure of Hem O−PH−NO (*25*). [e] Donor labile proton to nearest heteroatom acceptor, in Å. [f] X−H (donor)−Y (acceptor heteroatom) bond angle, in degrees. [g] Labile proton-O(water) distance, in Å, for the crystal structure (*25*).

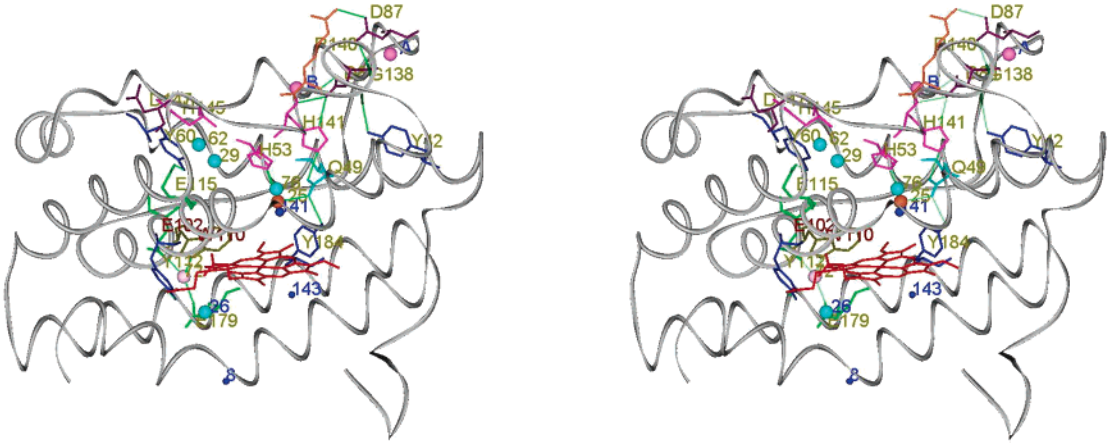

FIGURE 10: Stereoview of HemO−PH−NO showing the position of the relatively robust H-bonds and the water molecules sufficiently close to slowly exchanging H-bond donors to account for the observed steady-state NOEs and/or NOESY cross-peaks. The residues and water molecules are described in Table 3. The H-bond donors are color coded Arg140 NH and $N_\epsilon H$ (orange), His 141 NH and $N_\delta H$ (pink), Gly138 NpH (green), Gln49 $N_\epsilon H$ (pale blue) and $N_\epsilon H$ Trp110 (brown). The numbered blue spheres represent water molecules found in the HemO−PH−NO crystal structure (*25*) that account for the observed NOEs, while lettered spheres in pink represent water molecules observed solely by ^1H NMR.

HO-1, the α-biliverdin is transferred to the reductase upon forming a 1:1 complex with HO-1. The fate of the product α-biliverdin in bacterial HOs is unknown at this time (*3*). Last, the insertion of the cationic terminus of Arg208 to compensate the anionic 7-propionate salt bridge carboxylate should facilitate the reduction of the ligated oxy-complex.

The H-Bond Network. ^1H NMR studies of hHO−1−PH−CN (*30*, *33*) and HmuO−PH−CN (*31*) had shown that both possess an extended, largely iso-structural, network of H-bonds that involve some stronger than usual H-bonds (*54*, *66*, *67*), as reflected in the low-field bias for some dozen labile protons relative to the same groups in the majority of other folded proteins.[2] The chemical shifts for the low-field labile protons in HemO−PH−CN are listed in Table 3, where the correction for the δ_{dip}(calc) based on the magnetic axes determined above yields δ_{DSS}(dia*), the chemical shift the proton would exhibit in the absence of paramagnetism. It is δ_{DSS}(dia*), and not δDSS(obs) whose degree of low-field bias correlates with H-bond distance (*54*), and hence H-bond strength (*66*, *67*). Some NH low-field bias arises primarily from δ_{dip} (i.e., His23 and Asp24), while the OH of Tyr184 at 7.4 ppm experiences significant upfield δ_{dip} and heme ring current that suggest a stronger H-bond than indicated by δ_{DSS}-(obs). The Table also includes the likely acceptor(s) to those labile protons in robust H-bonds, as characterized by X−H..Y distances/angles in the crystal structure (*25*).

The peptide NHs of Arg140, His141, Asp147, and Gly138, as well as several side chain labile protons (Gln49 $N_\epsilon H$, the Tyr60 OH and Arg140 $N_\epsilon H$), exhibit lower field chemical shifts than those usually found in proteins[2] and reflect somewhat shorter (*54*) and hence stronger (*66*, *67*) than usual H-bonds. The shifts for the two His ring NHs (His53, His141) exhibit shifts typical of ordinary H-bonds. The H-bond described in Table 3 are part of an extended network in the distal pocket, as depicted in the stereoviews in Figure 10. This network includes two water molecules, one near His53 (detected in the crystal structure (*25*)) and another an acceptor to the Trp110 $N_\epsilon H$ (detected in the crystal structure (*25*) and

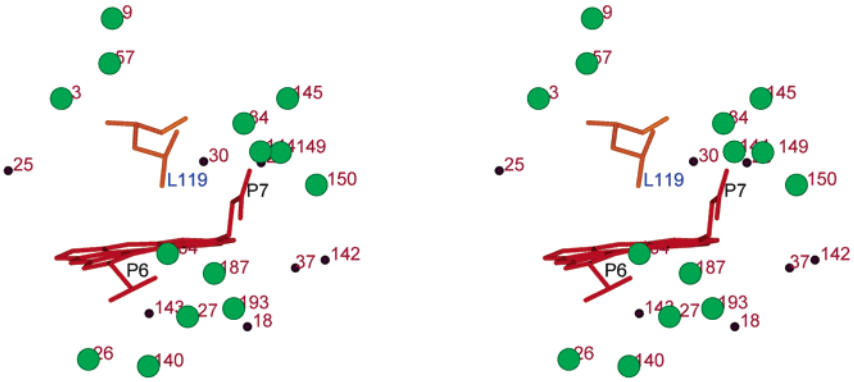

FIGURE 11: Stereoviews of the water molecules found near the heme and Leu119 in the crystal structure of reduced HemO−PH−NO (*25*). The heme is shown in red, and Leu119 is shown in orange. Small spheres represent water molecules near (∼5 Å) the heme positions 1−5 and 8; numerous water molecules closer (∼<4 Å) to Leu119, and the two propionates are shown as larger spheres (P6, P7 = 6-, 7-propionates, respectively).

by NMR (brown spheres), shown as pink spheres in Figure 10). The majority of the H-bonds are between two different secondary structural elements. The strong low-field bias of the NHs of Arg140 and His141 are rationalized by the Asp87 CO_2^- as acceptor, and this strong H-bond link is homolgous to that observed for Ala165/Phe160 to Asp92 in hHO-1 (*30*) and Gly159/Phe160 to Asp83 in HmuO (*26*, *31*). The remaining H-bonds do not have obvious homologues in HmuO and hHO-1.

Labile Proton Exchange and Dynamic Stability. Transfer of HemO−PH−CN from ^1H_2O to ^2H_2O leads to gradual loss of intensity of labile proton peaks in the low-field spectral window, (not shown; see Supporting Information). The approximate half-lives for exchange at 25 °C are included in Table 3. The exchange is slow enough ($\tau_{1/2}$ > 2 min) to detect six peptide NHs (His23, Asp24, Ala121, Gly138, Arg140, and His141), and two side chain NHs (N_ϵH Trp110 and N_δH of His141), the latter five of which were each shown to participate in the distal H-bond network. In addition, HemO−PH−CN NOESY spectra for one month in ^2H_2O exhibited the complete pattern of N_i−N_{i+1} cross-peaks for residues Tyr112-Ser117; the N_i−N_{i+1} cross-peaks for Ala114-Glu115 and Val186-Leu188 are still readily detected after 1 year in ^2H_2O (not shown). Similar ^1H_2O-^2H_2O conversion for hHO-1-PH−CN (*30*) and HmuO−PH−CN (*33*) showed the homologous distal (Gly143 in hHO-1, Gly139 in HmuO) and proximal helix (His25, Asp26 in hHO-1, His20, Glu21 in HmuO) are completely lost within 10 min, indicating $\tau_{1/2}$ < 3 min. Labile proton exchange, k_{ex}, in folded proteins occurs primarily through local transient unfolding (*68*), and the relative rates for isostructural labile protons in the two structures *i* and *j*, can be correlated with the relative dynamic stability, $\delta\Delta G$, where

$$\delta\Delta G = \Delta G^i - \Delta G^j = RT \ln k^i_{ex}/k^j_{ex} \qquad (5)$$

Hence, HemO−PH−CN exhibits significantly enhanced dynamic stability of both the proximal and distal helices by >2 kcal/mol, relative to those in HmuO and hHO-1. The enhanced dynamic stability of the proximal helix is further supported by the ready detection of the axial His ring N_δH in HemO−PH−CN, while the same proton for the axial His is not detectable at 25° for the other HO complexes (*30*, *31*, *33*). The more compact nature of the active site of HemO−PH−H_2O/NO (*4*, *24*, *25*) relative to either mammalian HOs (*17*, *19*, *21*−*23*, *36*) or HmuO (*26*) has already been noted in their crystal structures.

Magnetization Transfer from Water and Ordered Water Molecules. Saturation of the water resonance in steady-state NOE spectra, or the slice through the water signal in 2D "3:9:19" NOESY spectra, reveals significant magnetization transfer to both labile and nonlabile protons in HemO−PH−CN, as shown in Figures 3 and 4. If it can be demonstrated that this magnetization transfer to labile protons is faster than allowed by exchange of the labile proton, and there are no nearby protein labile protons that do exchange rapidly with bulk water; such NOEs or NOESY cross-peaks can be attributed to water molecules within the protein (*35*). The sign of the NOE, positive or negative, indicates (*35*) whether the water molecule tumbles (τ_r) like in liquid water (τ_r < 5 ns) or is partially immobilized with τ_r > 5 ns, respectively.

Magnetization transfer to eight slowly exchanging (k < 10^{-2} s^{-1}) labile protons in the steady-state NOE difference trace in Figure 3B or the water slices of a "3:9:19" NOESY spectrum in Figure 3C includes the peptide NHs of His23 and Asp24, (proximal helix), Ala122 (distal helix), Gly138, Arg140, and His141 (helix 8), and the side chain protons of Trp110 and His141. Inspection of the crystal structure fails to identify any other nearby enzyme labile protons that exchange rapidly with water, dictating that the magnetization transfer must result from NOEs by nearby, ordered water molecules (*35*). Since the size of the NOEs ∼−5 to −10% to the labile proton and selective T_1s (∼30 ms) are similar to those reported for both hHO−1−PH−CN (*32*) and HmuO−PH−CN (*31*), we conclude that the water is similarly located ∼4 Å from the protons exhibiting the NOEs. The stereoviews in Figure 10 that depict the H-bond network in HemO−PH−CN also show the positions of ordered water molecules (pale blue, numbered spheres) in the crystal structure of HemO−PH−NO (*25*) that can account for the observed NOEs/NOESY cross-peaks to the slowly exchanging H-bond donors. In the absence of any water molecules close enough to account for the NOEs to Arg140 and His141 NHs, we propose ordered water molecules A and B (pink lettered spheres in Figure 10). The water molecules are also described in Table 3.

Water also leads to small, but reproducible (∼3% negative) NOEs to all the resolved heme signals (except the much larger NOEs to the 7-propionate; see below) (3-CH_3, 2H_α, 7H_α (Figure 3B), and 8-CH_3 (Figure 3C) in steady-state NOE

difference spectra (Figure 3B) (as well as in 3:9:19 NOESY slices (Figure 3C)). In agreement with such observations, the crystal structure finds at least one water molecule close enough (<5 Å) to result in such small NOEs, as shown by small spheres in the stereoviews of the heme in Figure 11. Of greater interest are the much larger (10−15%) negative NOEs or NOESY cross-peaks to the 6-propionate H_α (Figure 3B) and H_βs (Figure 4B, 4C), as well as to the Leu119 C_βHs and $C_\delta H_3$s (Figure 4B, 4C). Inspection of the crystal structure of HemO−PH−NO reveals the presence of numerous water molecules close (∼<4 Å) to both the 6- and 7-propionates and the terminus of Leu119, as depicted in the large spheres in the stereoviews of the pyrrole B/C junction and Leu119, in Figure 11. The number and distances of water molecules to the 7- and 6-propionate H_βs in the crystal structure (*25*) are similar.

The much smaller water NOEs to the 7- than 6-propionate protons could result from the expulsion of these water molecules near the 7-propionate by the insertion of His207/Arg208 into the vicinity of pyrrole D. The model in Figure 9 indicates that the Arg208 terminus would overlap some of the water molecules near the 7-propionate. A less likely rationalization is that the ordered water molecules are more mobile (*35*) near the 7- than 6-propionate. Also to be considered is the possibility that the water molecules found near the 7-propionate in the crystal structure are, in fact, the more localized terminal atoms of Arg208 oriented into the heme pocket. Again, isotope labeling and much more extensive 2D/3D NMR, as well as mutagenesis, will provide a more definitive answer.

CONCLUSIONS

Solution ^{1}H NMR of the cyanide-inhibited, substrate bound heme oxygenase from *N. meningitidis* has allowed sufficient assignments and structural characterization by solely homonuclear ^{1}H 2D methods to demonstrate that the overall structure is strongly conserved in solution relative to that found in crystal structures (*24*, *25*) and that in cases where key distal residue orientations differ in the alternate crystal structures, the HemO−PH−CN structure always more closely resembled that possessing a diatomic, H-bond acceptor (HemO−PH−NO) than a monatomic H-bond donor (HemO−PH−H_2O) ligand. These results suggest that the orientation of Asn118, Leu119, Arg140 and 7-propionate side chain respond to the nature of the axial ligand. The orientation of the major magnetic axis dictates that the Fe−CN unit is tilted in the general direction of the α-meso-points, but to a lesser degree than in hHO-1 (*29*, *30*) or HmuO (*31*) complexes. An extended H-bond network is identified in the distal pocket that has limited homology to that previously described for hHO-1 and HmuO complexes, but appears to be similarly involved in stabilizing tertiary structure and ordering water molecules within the network. Proton lability reveals a tighter, more dynamically stable heme pocket than that found in other HOs. The detection of direct interaction between pyrrole D and two terminal residues, His207, and Arg208, not detected in the crystal structure, indicates that these two residues may form H-bond/salt-bridges to the Asp27 and 7-propionate carboxylates. The side chain reorientations and ordering of the C-terminal residues in the distal pocket closes the heme cavity appear to expel a series of water molecules near pyrrole D and may be involved in facilitating exit of the product from the cavity. With the resolution afforded by heteroatom labeling, the detailed structure of the C-terminal residues of the enzyme should be ideally addressable by solution NMR. The necessary steps to initiate these approaches are under study.

SUPPORTING INFORMATION AVAILABLE

One table (observed shifts and calculated dipolar shifts for assigned residues) and nine figures (steady-state NOEs, NOESY connections for relaxed/hyperfine-shifted residues, TOCSY spectrum, plot of δ_{dip}(calc) vs d[δ_{DSS}(obs)]/d[T^{-1}], dipolar contacts among helices, Curie plot for the heme resonances, and ^{1}H → ^{2}H exchange spectra). This material is available free of charge via the Internet at http://pubs.acs.org.

REFERENCES

1. Tenhunen, R., Marver, H. S., and Schmid, R. (1969) Microsomal heme oxygenase. Characterization of the enzyme, *J. Biol. Chem. 244*, 6388−6394.
2. Maines, M. D. (1988) Heme oxygenase: function, multiplicity, regulatory mechanisms, and clinical applications, *FASEB J. 2*, 2557−2568.
3. Yoshida, T., and Migita, C. T. (2000) Mechanism of heme degradation by heme oxygenase, *J. Inorg. Biochem. 82*, 33−41.
4. Wilks, A. (2002) Heme Oxygenase: Evolution, Structure, and Mechanism, *Antioxid. Redox Signal. 4*, 603−614.
5. Ortiz de Montellano, P. R., and Auclair, K. (2003) in *The Porphryin Handbook* (Kadish, K. M., Smith, K. M., and Guilard, R., Eds.) pp 175−202, Elsevier Science, San Diego, CA.
6. Schmitt, M. P. (1997) Utilization of host iron sources by Corynebacterium dihtheriae: identification of a gene whose product is homologous to eukaryotic heme oxygenases and is required for acquisition of iron from heme and hemoglobin *J. Bacteriol. 179*, 838−845.
7. Zhu, W., Willks, A., and Stojiljkovic, I. (2000) Degradation of heme in gram-negative bacteria: the product of the hemO gene of Neisseriae is a heme oxygenase *J. Bacteriol. 182*, 6783−6790.
8. Bullen, J. J., and Griffiths, E. (1999) in *Iron and Infection: Molecular, Physiological, and Clinical Aspects*, pp 87−213, John Wiley and Sons, New York.
9. Ratliff, M., Zhu, M., Deshmukh, R., Wilks, A., and Stojiljkovic, I. (2001) Homologues of Neisserial Heme Oxygenase in Gram-Negative Bacteria: Degradation of Heme by the Product of the pigA Gene of *Pseudomonas aeruginosa*, *J. Bacteriol. 183*, 6394−6403.
10. Wilks, A., and Schmitt, M. P. (1998) Expression and characterization of a heme oxygenase (HmuO) from Corynebacterium diphtheriae *J. Biol. Chem. 273*, 837−841.
11. Beale, S. I. (1994) Biosynthesis of open-chain tetrapyrroles in plants, algae, and cyanobacteria, *Ciba Foundation Symposium 180*, 156−168.
12. Ortiz de Montellano, P. R. (1998) Heme Oxygenase Mechanism: Evidence for an Electrophilic, Ferric Peroxide Species, *Acc. Chem. Res. 31*, 543−549.
13. Schuller, D. J. (2001) in *Handbook of Metalloproteins* (Messerschmidt, A., Huber, R., Poulos, T. L., and Wieghardt, K., Eds.) pp 317−327, John Wiley & Sons, Inc., New York.
14. Davydov, R. M., Yoshida, T., Ikeda-Saito, M., and Hoffman, B. M. (1999) Hydroperoxy-Heme Oxygenase Generated by Cryoreduction Catalyzes the Formation of α-*meso*-Hydroxyheme as Detected by EPR and ENDOR, *J. Am. Chem. Soc. 121*, 10656−10657.
15. Davydov, R., Kofman, V., Fujii, H., Yoshida, T., Ikeda-Saito, M., and Hoffman, B. M. (2002) Catalytic mechanism of heme oxygenase through EPR and ENDOR of cryoreduced oxy-heme oxygenase and its Asp 140 mutants *J. Am. Chem. Soc. 124*, 1798−1808.
16. Ortiz de Montellano, P. R. (1995) in *Cytochrome P450: Structure, Mechanism, and Biochemistry* (Ortiz de Montellano, P. R., Ed.) pp 245−304, Plenum Press, New York.

17. Schuller, D. J., Wilks, A., Ortiz de Montellano, P. R., and Poulos, T. L. (1999) Crystal structure of human heme oxygenase-1 *Nat. Struct. Biol. 6*, 860−867.
18. Lad, L., Wang, J., Li, H., Friedman, J., Bhaskar, B., Ortiz de Montellano, P. R., and Poulos, T. L. (2003) Crystal Structures of the Ferric, Ferrous, and Ferrous-NO Forms of the Asp140Ala Mutant of Human Heme Oxygenase-1: Catalytic Implications, *J. Mol. Biol. 330*, 527−538.
19. Sugishima, M., Omata, Y., Kakuta, Y., Sakamoto, H., Noguchi, M., and Fukuyama, K. (2000) Crystal structure of rat heme oxygenase-1 in complex with heme, *FEBS Lett. 471*, 61−66.
20. Sugishima, M., Sakamoto, H., Higashimoto, Y., Omata, Y., Hayashi, S., Noguchi, M., and Fukuyama, K. (2002) Crystal structure of rat heme oxygenase-1 in complex with heme bound to azide: Implication for regiospecific hydroxylation of heme at the α-*meso* carbon, *J. Biol. Chem.*, 45086−45090.
21. Sugishima, M., Sakamoto, H., Noguchi, M., and Fukuyama, K. (2003) Crystal Structures of CO-, CN-, and NO−Bound Forms of Rat Heme Oxygenase-1 (HO-1) in Complex with Heme: Structural Implications for Discrimination between CO and O2 in HO-1, *Biochemistry 42*, 9898−9905.
22. Lad, L., Schuller, D. J., Shimizu, H., Friedman, J., Li, H., Ortiz de Montellano, P. R., and Poulos, T. L. (2003) Comparison of the Heme-free and -bound Crystal Structures of Human Heme Oxygenase-1, *J. Biol. Chem. 278*, 7834−7843.
23. Sugishima, M., Sakamoto, H., Kakuta, Y., Omata, Y., Hayashi, S., Noguchi, M., and Fukuyama, K. (2002) Crystal Structue of Rat Apo-Heme Oxygenase-1 (HO-1): Mechanism of Heme Binding in HO-1 Inferred from Structural Comparison of the Apo and Heme Complex Forms, *Biochemistry 41*, 7293−7300.
24. Schuller, D. J., Zhu, W., Stojiljkovic, I., Wilks, A., and Poulos, T. L. (2001) Crystal structure of heme oxygenase from the Gram-negative pathogen *Neisseria meningitidis* and a comparison with mammalian heme oxygeanse-1, *Biochemistry 40*, 11552−11558.
25. Friedman, J. M., Lad, L., Deshmukh, R., Li, H. Y., Wilks, A., and Poulos, T. L. (2003) Crystal structures of the NO- and CO-bound heme oxygenase from Neisseriae meningitidis−Implications for O2 activation, *J. Biol. Chem. 278*, 34654−34659.
26. Hirotsu, S., Chu, G. C., Unno, M., Lee, D.-S., Yoshida, T., Park, S.-Y., Shiro, Y., and Ikeda-Saito, M. (2004) The Crystal Structures of the Ferric and Ferrous Forms of the Heme Complex of HmuO, a Heme Oxygenase of *Corynebacterium diphtheriae*, *J. Biol. Chem. 279*, 11937−11947.
27. Takahashi, S., Ishikawa, K., Takeuchi, N., Ikeda-Saito, M., Yoshida, T., and Rousseau, D. L. (1995) Oxygen-bound heme−heme oxygenase complex−evidence for a highly bent structure of the coordinated oxygen, *J. Am. Chem. Soc. 117*, 6002−6006.
28. Gorst, C. M., Wilks, A., Yeh, D. C., Ortiz de Montellano, P. R., and La Mar, G. N. (1998) Solution ^{1}H NMR investigation of the molecular and electronic structure of the active site of substrate-bound human heme oxygenase: the nature of the distal hydrogen bond donor to bound ligands, *J. Am. Chem. Soc. 120*, 8875−8884.
29. La Mar, G. N., Asokan, A., Espiritu, B., Yeh, D. C., Auclair, K., and Ortiz de Montellano, P. R. (2001) Solution ^{1}H NMR of the active site of substrate-bound, cyanide-ligated, human heme oxygenase. Comparison to the crystal structure of the water-ligated form, *J. Biol. Chem. 276*, 15676−15687.
30. Li, Y., Syvitski, R. T., Auclair, K., Wilks, A., Ortiz de Montellano, P. R., and La Mar, G. N. (2002) Solution NMR characterization of an unusual distal H-bond network in the active site of the cyanide-inhibited, human heme oxygenase complex of the symmetric substrate, 2,4-dimethyldeuteriohemin, *J. Biol. Chem. 277*, 33018−33031.
31. Li, Y., Syvitski, R. T., Chu, G. C., Ikeda-Saito, M., and La Mar, G. N. (2003) Solution ^{1}H NMR investigation of the active site molecular and electronic structures of the substrate-bound, cyanide-inhibited bacterial heme oxygenase from *C. diphtheriae*, *J. Biol. Chem. 279*, 6651−6663.
32. Syvitski, R. T., Li, Y., Auclair, K., Ortiz de Montellano, P. R., and La Mar, G. N. (2002) ^{1}H NMR detection of immobilized water molecules within a strong hydrogen-bonding network in the distal side of substrate-bound human heme oxygenase, *J. Am. Chem. Soc. 124*, 14296−14297.
33. Li, Y., Syvitski, R. T., Auclair, K., Ortiz de Montellano, P. R., and La Mar, G. N. (2003) Solution ^{1}H, ^{15}N NMR spectroscopic characterization of substrate-bound cyanide-inhibited, human heme oxygenase: water occupation of the distal cavity, *J. Am. Chem. Soc. 125*, 13392−13403.
34. Li, Y., Syvitski, R. T., Auclair, K., Ortiz de Montellano, P. R., and La Mar, G. N. (2003) ^{1}H NMR Investigation of the Solution Structure of Substrate-free Human Heme Oxygenase: Comparison to the Cyanide-inhibited, Substrate-bound Complex, *J. Biol. Chem. 279*, 10195−10205.
35. Otting, G. (1997) NMR studies of water bound to biological molecules, *Prog. NMR Spectrosc. 31*, 259−285.
36. Koenigs Lightning, L., Huang, H.-W., Moënne-Loccoz, P., Loehr, T. M., Schuller, D. J., Poulos, T. L., and Ortiz de Montellano, P. R. (2001) Disruption of an active site hydrogen bond converts human heme oxygenase-1 into a peroxidase, *J. Biol. Chem. 276*, 10612−10619.
37. Fujii, H., Zhang, X., Tomita, T., Ikeda-Saito, M., and Yoshida, T. (2001) A role for highly conserved carboxylate, Aspartate-140, in oxygen activation and heme degradation by heme oxygenase-1, *J. Am. Chem. Soc. 123*, 6475−6484.
38. Sambrook, J., Fritsch, E. F., and Maniatis, T. (1989) *Molecular Cloning*: *A Laboratory Manual*, Cold Spring Harbor Laboratory Press, Cold Spring Harbor, NY.
39. Lowry, O. H., Rosebrough, N. J., Farr, A. L., and Randall, R. J. (1951) Protein measurement with the folin phenol reagent *J. Biol. Chem. 193*, 265−275.
40. Johnston, P. D., Figueroa, N., and Redfield, A. G. (1979) Real-time solvent exchange studies of the imino and amino protons of yeast phenylalanine transfer RNA by Fourier transform NMR *Proc. Natl. Acad. Sci. U.S.A. 76*, 3130−3134.
41. Piotto, M., Sandek, V., and Sklenar, V. (1992) Gradient-tailored excitation for single quantum NMR spectroscopy of aqueous solutions, *J. Biomol. NMR 2*, 661−666.
42. Gupta, R. K. (1976) Dynamic Range Problem in Fourier Transform NMR. Modified WEFT Pulse Sequence, *J. Magn. Reson. 24*, 461−465.
43. Jeener, J., Meier, B. H., Bachmann, P., and Ernst, R. R. (1979) Investigation of Exchange Processes by Two-Dimensional NMR Spectroscopy, *J. Chem. Phys. 71*, 4546−4553.
44. Griesinger, C., Otting, G., Wüthrich, K., and Ernst, R. R. (1988) Clean TOCSY for ^{1}H Spin System Identification in Macromolecules, *J. Am. Chem. Soc. 110*, 7870−7872.
45. Bax, A., and Davis, D. G. (1985) Mlev-17-based two-dimensional homonuclear magnetization transfer spectroscopy, *J. Magn. Reson. 65*, 355−360.
46. Emerson, S. D., and La Mar, G. N. (1990) Solution Structural Characterization of Cyano Met-Myoglobin: Resonance Assignment of Heme Cavity Residues by 2D NMR, *Biochemistry 29*, 1545−1555.
47. La Mar, G. N., Satterlee, J. D., and de Ropp, J. S. (1999) in *The Porphyrins Handbook* (Kadish, K. M., Smith, K. M., and Guilard, R., Eds.) pp 185−298, Academic Press, San Diego.
48. Williams, G., Clayden, N. J., Moore, G. R., and Williams, R. J. P. (1985) Comparison of the Solution and Crystal Structures of Mitochondrial Cytochrome *c*. Analysis of Paramagnetic Shifts in the Nuclear Magnetic Resonance Spectrum of Ferricytochrome *c*, *J. Mol. Biol. 183*, 447−460.
49. Bundi, A., and Wüthrich, K. (1979) ^{1}H NMR Parameters of the Common Amino Acid Residues Measured in Aqueous Solutions of the Linear Tetrapeptides H-Gly-Gly-X−L-Ala-OH, *Biopolymers 18*, 285−297.
50. Wishart, D. S., Sykes, B. D., and Richards, F. M. (1991) Relationship Between Nuclear Magnetic Resonance Chemical Shift and Protein Secondary Structure, *J. Mol. Biol. 222*, 311−333.
51. Neal, S., Nip, A. M., Zhang, H., and Wishart, D. S. (2003) Rapid and accurate calculation of protein ^{1}H, ^{13}C, and ^{15}N chemical shifts, *J. Biomol. NMR 26*, 215−240.
52. Cross, K. J., and Wright, P. E. (1985) Calibration of Ring-current Models for the Heme Ring, *J. Magn. Reson. 64*, 220−231.
53. Hernández, G., Wilks, A., Paolesse, R., Smith, K. M., Ortiz de Montellano, P. R., and La Mar, G. N. (1994) Proton NMR Investigation of Substrate-bound Heme Oxygenase: Evidence for Electronic and Steric Contributions to Stereoselective Heme Cleavage, *Biochemistry 33*, 6631−6641.
54. Wagner, G., Pardi, A., and Wüthrich, K. (1983) Hydrogen Bond Length and ^{1}H NMR Chemical Shifts in Proteins, *J. Am. Chem. Soc. 105*, 5948−5949.
55. La Mar, G. N., and de Ropp, J. S. (1993) NMR Methodology for Paramagnetic Proteins, *Biol. Magn. Reson. 18*, 1−79.
56. Wüthrich, K. (1986) *NMR of Proteins and Nucleic Acids*, Wiley & Sons, New York.

57. Qin, J., and La Mar, G. N. (1992) Complete Sequence-specific ^{1}H NMR Resonance Assignment of Hyperfine-shifted Residues in the Active Site of a Paramagnetic Protein: Application to *Aplysia* Cyano-metmyoglobin, *J. Biomol. NMR 2*, 597−618.
58. Shokhirev, N. V., and Walker, F. A. (1998) The Effect of Axial Ligand Plane Orientation on the Contact and Pseudocontact Shifts of Low-spin Ferriheme Proteins, *J. Biol. Inorg. Chem. 3*, 581−594.
59. Shokhirev, N. V., and Walker, F. A. (1995) Analysis of the Temperature Dependence of the ^{1}H Contact Shifts in Low-Spin Fe(III) Model Hemes and Heme Proteins: Explanation of "Curie" and "Anti-Curie" behavior within the Same Molecule, *J. Phys. Chem. 99*, 17795−17804.
60. La Mar, G. N., Kolczak, U., Tran, A.-T., and Chien, E. (2001) Solution ^{1}H NMR characterization of axial interactions of the proximal and distal His in the cyanomet complexes of the isolated chains and 65 kDa intact tetramer of human hemoglobin, *J. Am. Chem. Soc. 123*, 4266−4274.
61. Nguyen, B. D., Xia, Z., Yeh, D. C., Vyas, K., Deaguero, H., and La Mar, G. (1999) Solution NMR Determination of the Anisotropy and Orientation of the Paramagnetic Susceptibility Tensor as a Function of Temperature for Metmyoglobin Cyanide; Implications for the Population of Excited Electronic States, *J. Am. Chem. Soc. 121*, 208−217.
62. Emerson, S. D., and La Mar, G. N. (1990) NMR Determination of the Orientation of the Magnetic Susceptibility Tensor in Cyano Met-Myoglobin: A New Probe of Steric Tilt of Bound Ligand, *Biochemistry 29*, 1556−1566.
63. Caignan, G. A., Deshmukh, R., Wilks, A., Zeng, Y., Huang, H.-w., Moenne-Loccoz, P., Bunce, R. A., Eastman, M. A., and Rivera, M. (2002) Oxidation of heme to β- and δ-biliverdin by *Pseudomonas aeruginosa* Heme Oxygenase as a Consequence of an Unusual Seating of the Heme, *J. Am. Chem. Soc. 124*, 14879−14892.
64. Friedman, J., Lad, L., Li, H., Wilks, A., and Poulos, T. L. (2004) Structural Basis for Novel δ-Regioselective Heme Oxygenation in the Opportunistic Pathogen *Pseudomonas aeruginosa*, *Biochemistry 43*, 5239−5245.
65. Fujii, H., Zhang, X., and Yoshida, T. (2004) Essential Amino Acid Residues Controlling the Unique Regioselectivity of Heme Oxygenase in *Pseudomonas aeruginosa*, *J. Am. Chem. Soc. 126*.
66. Jeffrey, G. A. (1997) *An Introduction to Hydrogen Bonding*, Oxford University Press, New York.
67. Mildvan, A. S., Harris, T. K., and Abeygunawardana, C. (1999) Nuclear Magnetic Resonance Methods for the Detection and Study of Low-Barrier Hydrogen Bonds on Enzymes, *Methods Enzymol. 308*, 219−245.
68. Englander, S. W., and Kallenbach, N. R. (1984) Hydrogen exchange and structural dynamics of proteins and nucleic acids, *Quart. Rev. Biophys. 16*, 521−655.

BI049438S